FACULTY OF SCIENCE AND TECHNOLOGY

MASTER'S THESIS

Study program/specialization: Structural and Mechanical Engineering	The spring semester, 2023 Open
Author: Katrine Idsø	
Supervisor at UiS: Associated Professor Yanyan Sha Co-supervisor: PhD Martin Kristoffersen, NTNU External supervisor(s): PhD student Mathias Egeland Eidem, NPRA	
Thesis title: Numerical investigation of blast and fire response of secondary tunnel structures	
Credits (ECTS): 30	
Keywords: Blast, Structural response, SFTB, Element erosion, LS-DYNA	Pages: 66 + Appendix: 6 Stavanger, 15.06.23

Acknowledgements

This thesis marks the culmination of my master's degree in Structural and Mechanical Engineering at the University of Stavanger, Norway. Thus, I would like to take this opportunity to extend my heartfelt appreciation to all those who have played a significant role in shaping my academic journey during the past five years and have provided invaluable support throughout the process of writing this master's thesis.

I am deeply grateful to my supervisor, Yanyan Sha, for his guidance, support, and accessibility. His expertise in LS-DYNA and valuable insights greatly contributed to the development of the model.

I would also like to express my appreciation to my co-supervisor, Martin Kristoffesen, for his significant contributions to both the model development and the execution of this study. His knowledge and understanding of the subject matter, as well as his expertise in LS-DYNA, were invaluable throughout the past six months.

I extend my thanks to Mathias Egeland Eidem, my external supervisor from the Norwegian Public Roads Administration, for providing relevant information and insights that enriched my research.

I am grateful to DYNAMORE and Axel for their support in the LS-DYNA model development and for providing an introduction course.

I am grateful to my fellow classmates for their support and engaging discussions during the writing process. Special thanks to Ida Moen for being an exceptional companion in navigating the challenges of LS-DYNA.

I would like to express my heartfelt appreciation to my partner for his unwavering support throughout my academic journey, especially during the last six months. His encouragement and understanding have been invaluable.

Finally, I want to thank my family for their constant support over the past five years. I extend a special thanks to my brother for proofreading the final version of this thesis.

Abstract

Submerged Floating Tube Bridges (SFTB) are evaluated as potential fixed links in the Ferry-Free E39 project led by the National Public Road Administration (NPRA). However, the risk of internal explosions and the impact of fire on these structures are major concerns that must be addressed. Such events pose significant threats to the structural integrity and the safety of individuals and property. Therefore, it is crucial to thoroughly investigate and comprehend the structural response of the external and internal components of the SFTB when exposed to blast loading and the combination of blast load and fire.

The objective of this thesis was to investigate the structural response of internal structures in an SFTB to blast loading and the combined effect of blast loading and fire. LS-DYNA software was utilized to explore various scenarios, including different charge sizes of TNT, reinforcement presence, and consideration of pre-existing damage. The outcomes were a combination of anticipated and unforeseen results, particularly regarding the observed visual damage attributed to element erosion. A comprehensive preliminary study was conducted to ensure the reliability and accuracy of the material and blast models. This initial investigation aimed to identify any potential design constraints or limitations, thus establishing a robust foundation for the subsequent analysis.

Contents

List of Figures

List of Tables

1 Introduction

1.1 Background

The Norwegian Public Road Administration (NPRA) has an ambitious intervention plan along the E39 European road along the west coast of Norway. The highway E39 route goes all the way from Kristiansand in the southern part of Norway to Trondheim in the middle part of Norway, as illustrated in Figure 1.1. The total length of this route is 1100 km and takes approximately 21 hours to travel [1]. The main reason for the route's lengthy duration is the seven ferry crossings. By replacing these ferries with fixed links it is possible to travel the route in 13 hours [1]. More than 60% of the national export values are produced and exported through this part of Norway [10]. The west coast is also known for its lengthy duration between schools, hospitals, and job sites. By conducting the Ferry-Free E39 project the travel time will be reduced and the roads in this area will be improved [10] '

Figure 1.1: Highway E39 from Kristiansand to Trondheim [1].

The seven fjords are wide and deep, which makes fixed links challenging. If all the seven fjords were to be linked with bridges, these bridges would be the deepest and longest bridges ever made [1]. Technology from the Norwegian off-shore industry may be used for this purpose, especially the technology from the floating oil platforms. This technology may come in handy for constructions like floating bridges and Submerged Floating Tube Bridges (SFTB), which is the structure of focus in this thesis.

During the service life of an SFTB, it must be able to withstand many different types of

impact loads, such as explosions and fire. Explosions can occur as accidents or terrorist attacks. Incidents like this may lead to severe injuries, loss of life and property, and damage to tunnel structures.

While extensive research has been conducted on the response of the main tunnel structure to blast loads ([11]), there has been limited focus on the secondary structures. This limited attention can be attributed to traditional Norwegian road tunnels' lack of secondary structures, making it less relevant for these specific cases. However, it remains crucial to thoroughly understand the dynamic behavior exhibited by secondary structures when subjected to explosions. Additionally, it is essential to acknowledge that explosion incidents can lead to or be accompanied by fires within the tunnel. The influence of heat on the residual strength of reinforced concrete is significant, underscoring the necessity of studying the response of secondary structures under combined explosion and fire loading conditions.

1.2 Scope of work

The aim of this thesis is to investigate the dynamic response of the secondary structures in SFTBs with a circular cross section. The research approach involves conducting numerical simulations of explosions with different charge sizes on the tunnel secondary structures using a finite element method model implemented in LS-DYNA software. As a student, LS-DYNA was a new tool that had to be learned before proceeding with the main model and simulations. The simulations were carried out with and without reinforcement and the influence of fire.

The primary objective of this thesis is to advance the understanding of the dynamic behavior displayed by secondary structures in SFTBs under the effects of blast loading and fire. The analysis of the structural response primarily focuses on parameters such as the overall displacement of the deck, nodal displacement, Von Mises stress, and effective plastic volumetric strain. These key metrics are compared to discern the variations in the structural response under different conditions.

1.3 Limitations

In conducting this research, certain limitations were encountered that should be acknowledged. Utilizing LS-DYNA software posed a challenge due to the researcher's limited prior experience. As a result, a considerable amount of time was required to familiarize oneself with the software's functionalities and modeling techniques. Consequently, the modeling process was time-consuming, limiting the number of simulations executed within the available time frame.

Additionally, the observed results from the fire damaged model did not fully align with the initial expectations. Despite significant reductions in material strength, the model did not exhibit the anticipated level of damage. This can be attributed to the researcher's limited experience in using the pre-existing damage parameter input and by not considering the complex interdependencies of parameters in the material model. As a result, the reliability and accuracy of the results were compromised. Future studies should address these limitations by improving expertise in simulating pre-existing damage and accounting for parameter interdependencies to enhance the predictive capabilities of simulations.

Nevertheless, despite these limitations, this research provides valuable insights into the blast resistance of the internal constructions in an SFTB.

1.4 Structure of the thesis

Table 1.1: Structure of the thesis

Structure of the thesis	
Chapter 2	Presents a comprehensive review of the existing literature related to the research topic
Chapter 3	Presents a brief introduction to the blast loading theory
Chapter 4	Presents a preliminary study for the material model and blast model utilized in the thesis
Chapter 5	Presents the numerical setup of the intact SFTB and the results from the simulations
Chapter 6	Presents the numerical setup of the SFTB with the impact of fire, and the results from the simulation
Chapter 7	Discussing the results from Chapter 5 and Chapter 6
Chapter 8	Conclusion and further work

2 Literature Review

The topic of Submerged Floating Tube Bridges subjected to blasting is rather complex, which is why it is essential to get a good overview of previous research before starting new research.

The safety of tunnel structures subjected to internal explosions has attracted more attention in the past decades [7, 11–14]. Tunnel structures may be subjected to intentional explosions from terrorist attacks, accidental explosions from vehicle collisions, or transportation of flammable goods. Therefore, it is essential to understand the dynamic response of both the main tunnel structure and the secondary structures. Moreover, explosion accidents may lead to or be accompanied by fires in the tunnel. This thesis investigates the response of secondary tunnel structures under combined blast and fire loading.

Existing studies have primarily concentrated on the main tunnel structure under diverse circumstances and cross sections. For instance, Chakraborty et al. (2014) [14] investigated various tunnel lining materials under internal blast when the tunnel was situated in sandy soil. LI et al. (2022) [15] investigated BLEVE energy and over pressure inside a tunnel using two distinct cross sections. Mussa et al. (2017) [16] conducted numerical research on the relationship between explosive charge weight, tunnel lining thickness, and burial depth. Another important research paper for this thesis is by Kristoffersen et al. (2019) [11], which examined the dynamic response of an SFTB subjected to internal blast loading with both circular and rectangular cross sections. For this thesis, the circular cross section investigated by Kristoffersen et al. is also utilized, focusing on the secondary structures instead of the primary tunnel structure.

The field of research regarding the dynamic response of secondary tunnel structures subjected to blast loading is not as thoroughly examined. In the article by Kristoffersen et al. [11], the secondary constructions were considered and examined, but, as previously mentioned, the main construction was of most interest. In the study by CHENG et al. (2022) [17], the relevant research on the effects of internal explosions on secondary structures of tunnels and adjacent engineering structures was reviewed. The review concluded that the previous investigations of the response of secondary structures were insufficient and emphasized the need for further research in this area.

The existing research on the combined effects of blast loading and fire on tunnel structures is also limited ([13, 18–20]). Previous studies have predominantly focused on either blast loading or fire damage in reinforced concrete (RC) structures or elements ([21, 22]). Some research has explored the combination of blast and fire effects on RC elements like walls and columns ([23, 24]). However, there is a lack of comprehensive research specifically addressing the response of secondary tunnel structures to the combined influence of blast and fire.

To ensure the accuracy and reliability of the selected material and blast models, a validation process was carried out by conducting a numerical investigation of the blast response of a concrete pipe. The experimental data used for validation were obtained from a research paper by Kristoffersen et al. [7], where they performed experimental tests on a concrete pipe subjected to blast loading using C-4 explosives. By comparing the numerical simulation results obtained in this thesis with the experimental data from the research paper, the validity of the chosen material and blast models could be assessed. This validation process enhances the confidence in the models used in this thesis and provides a basis for further analysis and interpretation of the numerical simulations.

3 Theory

3.1 Submerged Floating Tube Bridge

The fjords along the E39 European road are wide and deep, therefore NPRA is evaluating special structures as alternative crossings. One alternative solution is the Submerged Floating Tube Bridges (SFTB), a submerged structure floating below the sea level [10]. Due to the characteristics of the Norwegian fjords the required fixed links along E39 are proven to be challenging [10]. There are fjords along the E39 that will have traditional fixed links like bridges, but some fjords with extreme depth (up to 1300 m) and length (up to 6 km) will require new technology [10].

For short crossings, it would be enough to connect the SFTB with the shores, but for longer crossings like the ones along the E39, this is not sufficient to provide the necessary stability [10]. By using pontoons (see Figure 3.1a) or tethers (see Figure 3.1b), this can be achieved. Tethers are the same type of structures used in the offshore industry in Norway [10]. By using tethers the tunnel will be totally submerged, which means that there will be no risk of ship collision and no visual impact, but it is dependent on the soil characteristics [10]. The pontoons, on the other hand, are floating on the sea surface, which leads to a higher risk of being subjected to both local and overall damage due to ship collision [25].

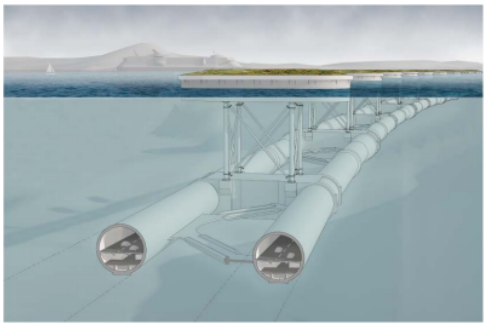

(a) SFTB with pontoons [10].

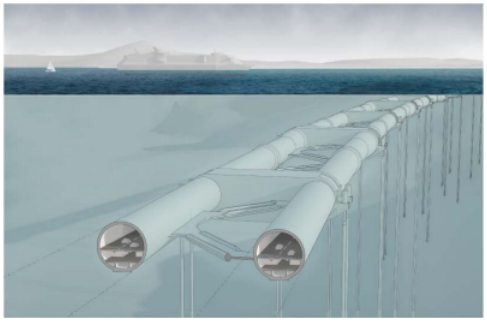

(b) STFB with tethers [10].

The North Sea and the Norwegian Sea have a big impact on the Norwegian coast, with extreme weather conditions that can affect the coastline throughout the year [10]. These extreme weather conditions have been registered with strong winds, high waves, and

severe currents. Therefore, the positioning of the structure is very important. Taking Bjørnafjord as an example, the position for the crossing was chosen due to some islands that are shielding the area, which reduces the open-sea conditions [10].

A potential hazard for structures such as an SFTB is internal blast loading. An internal blast loading can be done by accident or intended. Either way, an internal blast loading could be devastating for the structure. However, the major concern is blast loading and fire from accidents involving tankers transporting dangerous cargo, such as liquid natural gas or gasoline, or from potential terrorist attacks [11]. The blast phenomena will be further discussed and investigated in the next section.

3.2 Blast Loading

This section will give a brief introduction to the blast phenomena.

3.2.1 General definition of Blast Loading

A blast may be defined as a pressure disturbance caused by a sudden release of energy. As a product of this sudden energy release, there will usually be generated high temperatures and released high-pressure gases. These high-pressure gases are called shock waves, which is a region of highly compressed air that radiates spherically away from an explosive source [26]. As this region of compressed air passes by a given point in space there is created an overpressure and a dynamic pressure. Overpressure is also known as side-on pressure, static pressure, or gauge pressure, and is defined as the gas pressure caused by compression or heating of gas [27]. While dynamic pressure is also known as gust or differential pressure and is defined as the pressure caused by the motion of the gas [27].

3.2.1.1 TNT Equivalency

The nature of blast waves from all condensed high explosives is quite similar. This enables the calculation of an equivalent charge weight of the explosive that would be needed to generate a blast effect similar to a spherical Trinitrotoluene (TNT) explosive [3]. The Effect of the energy output for a different explosive material relative to TNT can be computed as follows [3]:

$$W = (\frac{\Delta H_{EXP}}{\Delta H_{TNT}})W_{EXP} \tag{3.1}$$

Where:

W = TNT equivalent charge weight

ΔH_{EXP} = Heat of detonation of explosive in question

ΔH_{TNT} = Heat of detonation of TNT

W_{EXP} = Weight of explosive in question

3.2.2 Classification

This section will provide a brief introduction to the most relevant explosion classification for this thesis.

3.2.2.1 Chemical Explosion

For a chemical explosion to happen it requires a chemical reaction, which could be a combustion reaction, a decomposition reaction, or some other rapid exothermic reaction [28]. Chemical explosions can occur in vapor, liquid or solid phases. Chemical explosions that occur in the liquid or solid phase are also called condensed-phase explosions. Due to the high energy density in the material, these are significant. Propagating reactions are classified as detonations or deflagrations, depending on how fast the reaction front propagates through the unreacted mass [28]. TNT is an example of a detonation reaction. The reaction front of this type of chemical explosion moves equal to or faster than the speed of sound in the unreacted medium [28].

3.2.3 External Blast Environment

Blast waves pose a serious threat to structures. Damage to critical infrastructures, such as energy and transport sectors, like power plants, bridges, or tunnels, may be particularly harmful and crippling to society. A blast wave is formed by a sudden release of energy, and the blast wave propagates freely until it encounters an object and is then reflected off that object. Multiple objects and closed spaces may create wave interactions and

local pressure peaks - this wave propagation and how it acts in different environments is essential to understand.

3.2.3.1 Free Air Burst

When a detonation occurs close to and above a protective structure such that no amplification of the initial shock wave occurs between the explosive source and the protective structure, the blast load acting on the structure is a free air burst [2]. This phenomenon is illustrated in Figure 3.2

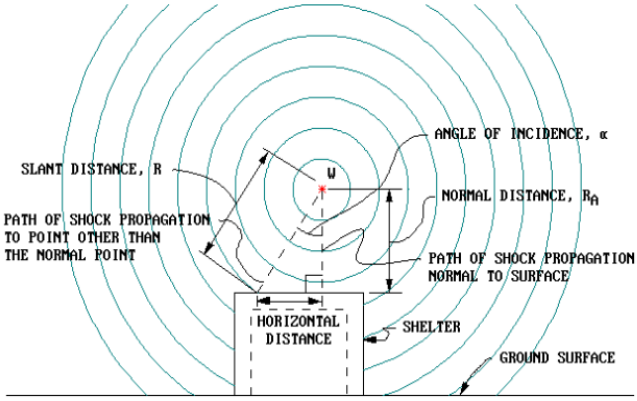

Figure 3.2: Free-Air Burst Environment [2].

3.2.3.2 Air Burst

The air burst environment is produced by a detonation that occurs above the ground surface and at a certain stand-off distance away from the protective structure. The initial shock wave propagates away from the produced explosion, hitting the ground surface before reaching the structure [2]. As the shock wave continues to propagate outward

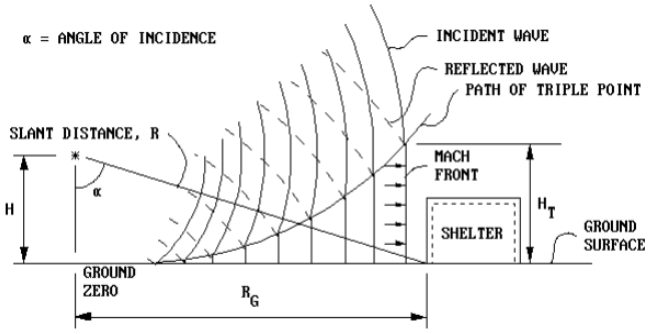

Figure 3.3: Air Burst Environment [2].

along the ground surface, a front known as a Mach front (see Figure 3.3) is formed by the interaction of the initial wave (incident wave) and the reflected wave (reflection from the ground surface) [2].

3.2.3.3 Surface Burst

An explosion located very near or on the ground surface is considered to be a surface burst. The ground surface reflects and reinforces the initial wave from the explosion by producing a reflected wave [2]. Unlike the air burst, the reflected wave from the surface burst merges with the incident wave at the point of detonation and forms a single wave as illustrated in Figure 3.4. The produced wave is very similar to the Mach front from the air burst but essentially hemispherical in shape [2].

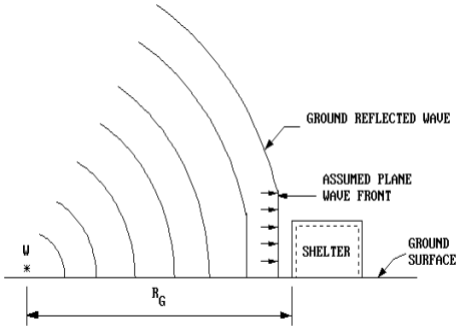

Figure 3.4: Surface Burst Environment [2].

3.2.4 Reflection of Blast Waves

The reflected wave is a term used to describe the wave that is reflected of a surface. The velocity of the reflected wave is higher than the velocity of the incident wave. This is because the air has already been heated and compressed, resulting in less air resistance for the reflected wave [26]. Waves reflected by a rigid surface, such as the ground, have the potential to catch up to and merge with the incident wave and form a Mach front as sketched in Figure 3.3 [26]. If the incident angle of the blast wave (α) changes, so will the reflected pressure. When the blast load is head-on, α=0°, the pressure is maximized, and when the blast load is side-on, α=90°, the pressure is minimized. For angles ranging between 40° and 55°, the reflected pressure will be moderate. It is typically within this range of angles that the Mach front is formed [29].

3.2.5 Internal Explosions

Road tunnels are critical components in the road transportation network and may be subjected to blast loading during their service life. An explosion inside a tunnel is referred to as an internal explosion and can be further categorized as an internal air explosion (i.e explosion in the air space in the tunnel) and an internal contact explosion (i.e explosion close to the wall or the surface in the tunnel) [13]. For the scenario of internal air explosion, when the incident wave encounters the closest tunnel wall the reflected and transmitted blast waves are formed at the same time [13]. The reflected wave will continue to propagate in the tunnel, and the transmitted wave will continue to propagate outwards in the medium around the tunnel [13]. As the reflected waves continue to reflect from the walls in the tunnel, there will be formed multiple pressure peaks. Furthermore, there can also be formed Mach fronts at the closest tunnel walls. The generated Mach front from an internal air explosion is very similar to a Mach front generated from an internal contact explosion. However, unlike the air explosion, the reflected waves from the contact explosion will merge with the incident wave, creating unified waves with a hemispherical shape, resulting in a higher blast pressure and impulse [13].

3.2.6 Engineering Practices

This section introduces some common engineering for design against blast loads.

3.2.6.1 Planer Wave Assumptions

While there is a plethora of possible blast load cases to consider, a typical blast load design procedure assumes a planar blast wave incoming from a detonation. This blast wave is generated by an explosive charge of known mass (W) at a specific distance (R) from the structure [3]. The stand-off distance (Z) can be determined using the Hopkinson-Cranz or "cube-root" scaling law, as shown in Equation 3.2. This equation allows for estimating the appropriate distance from the blast source based on the charge mass [3].

$$Z = \frac{R}{\sqrt[3]{W}} \tag{3.2}$$

The concept of the scaling laws, illustrated in Figure 3.5, further aids in blast wave analysis. According to the Hopkinson-Cranz scaling law, if the size of the explosive source, the distance from the source, and the blast wave characteristics (amplitude, duration, and impulse) are all scaled proportionally, the response of the structure will remain the same [3]. In other words, the blast wave's effect on the structure will be consistent regardless of the scaling of these properties. However, it is crucial to ensure that the blast environments being compared are comparable, and the shock wave generated is spherical for these scaling laws to be applicable effectively [3].

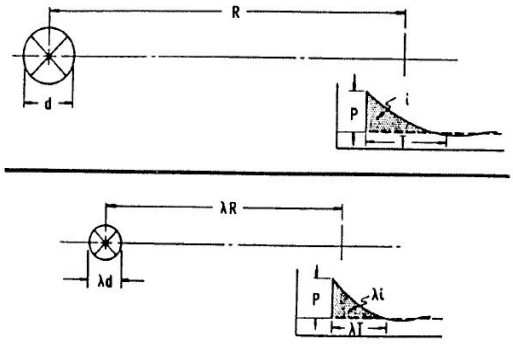

Figure 3.5: Hopkinson-Cranz blast wave scaling [3].

Additionally, simplified methods such as the method developed by Kingery and Bulmash (discussed in Section 3.2.7.1) are commonly used to predict blast wave characteristics [30]. It is important to note that these methods are based on ideal blast conditions and should only be used within the range of available experimental data.

3.2.6.2 Pressure-Impulse Diagram

The exact magnitude and duration of a blast wave can be difficult to determine and, in most cases unknown. The Pressure-Impulse diagram is an effective tool that easily assesses the structural response to a specific load in the early design phase.

By defining a maximum displacement or damage level, the P-I-diagram will demonstrate the combination of load and impulse that may cause structural failure or damage. During the second world war, the P-I diagram was developed to study the bombing-induced damage to residential houses. Later it was found helpful in analyzing elastic single degree of freedom (SDOF) models [4]. Due to their simplicity and low computational cost, SDOF models are typically used to assess the dynamic structural response caused by severe

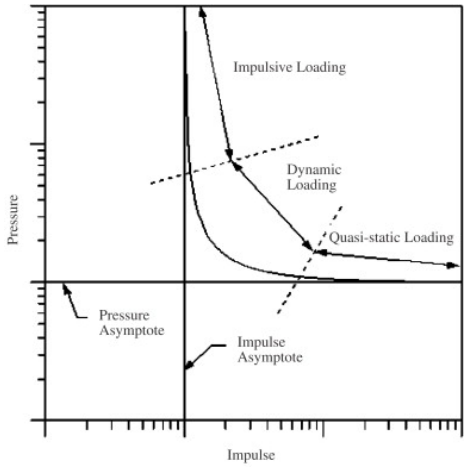

Figure 3.6: An example of a P-I diagram [4].

dynamic loads [31].

Figure 3.6 shows a typical example of a P-I diagram. The pressure asymptote and the impulse asymptote are predefined as the limiting values for each parameter. Loads with a concise duration relative to the structure's natural frequency are called impulse loading. The structural response is sensitive to the associated impulse, not necessarily the peak pressure [4]. The impulse asymptote defines the minimum impulse required to reach a particular level of damage and crosses the pressure asymptote at high pressure, as illustrated in Figure 3.6. On the contrary, if the load duration is much longer than the structure's natural frequency, the load is called quasi-static loading. If this is the load case, then the response will become insensitive to impulse but very sensitive to the peak pressure. The pressure asymptote then represents the minimum peak pressure required to reach the particular level of damage [4].

3.2.7 Prediction of Blast Load

To estimate or calculate the response of an object or a structure to the effect of an explosion, it is necessary to know the explosion parameters. Among these parameters, the most critical are peak overpressure (q_0), positive phase duration, and positive phase impulse (i). The positive phase impulse can usually be calculated from the blast curve (Figure 3.7) and depends on the overpressure and positive duration [5]. Knowledge of the blast parameters becomes essential by defining the primary load of buildings or structures.

Various methods can be employed to determine the explosion parameters, including

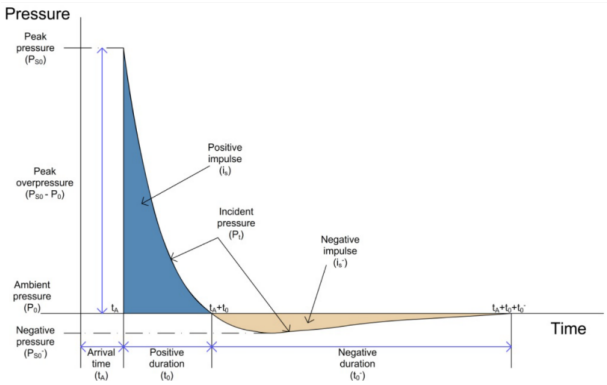

Figure 3.7: Idealized pressure-time variation from free air burst [5].

empirical, semi-empirical, and numerical methods. Empirical methods rely on correlations with experimental data and are limited by the experiments' range [5]. As a result, their accuracy generally decreases with increasing distance from the source of the explosion. Semi-empirical methods utilize simplified models of physical phenomena and attempt to capture essential physical processes in a simplified manner [5]. These methods rely on extensive experimental data, and their predictive accuracy is generally better than that of empirical methods [5].

3.2.7.1 Empirical Method

The most commonly used empirical method for predicting blast loading is the experimental data obtained by Kingery and Bulmash. By collecting data from the literature on explosions in idealized conditions and by using Hopkinson-Cranz scaling, Kingery and Bulmash curve-fitted the data high-order polynomials as a function of the TNT-equivalent blast parameters [30]. These equations predict blast properties such as peak pressure, impulse, and duration. However, as mentioned in Section 3.2.6.1, the data obtained by Kingery and Bulmash are based on experiments in highly idealized conditions, which is why these equations should not be used outside the range of experimental data, such as for complex blast environments. The curve-fitted data obtained by Kingery and Bulmash for free air burst (a) and surface burst (b) are illustrated in Figure 3.8.

CONWEP is short for Conventional Weapons and is a blast model available in ABAQUS and LS-DYNA. The CONWEP approach is based on the experimental data obtained by Kingery and Bulmash. A scaled distance based on the distance of the loading surface from the source of the explosion and the amount of explosives is used in the CONWEP

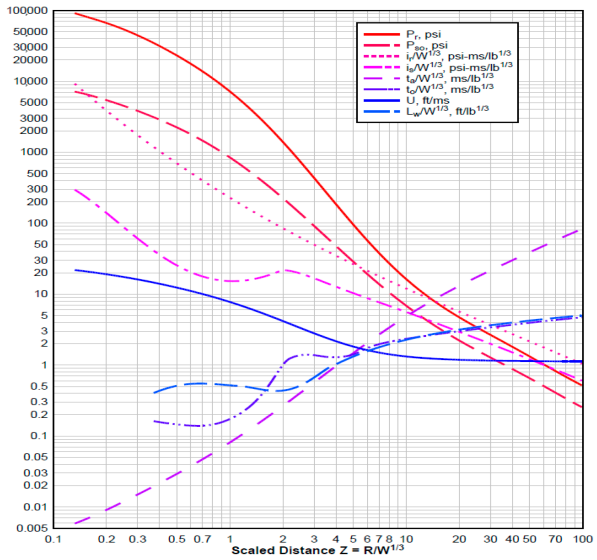

(a)

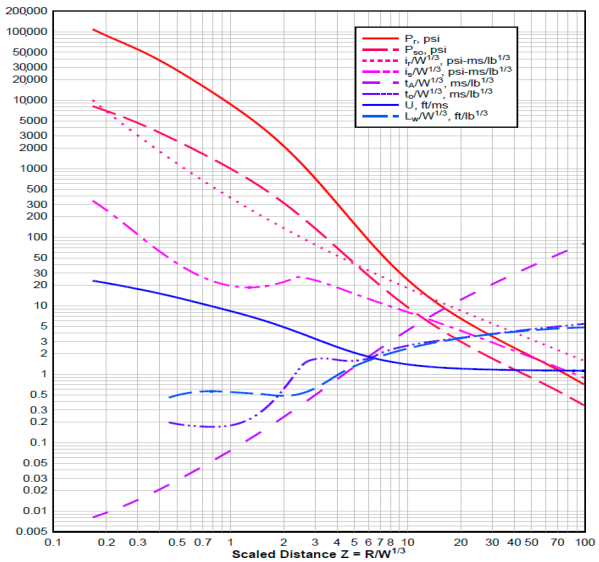

(b)

Figure 3.8: Kingery and Bulmash blast parameters for TNT [2].

model [32]. For a given scaled distance, the model automatically provides the following empirical data: maximum overpressure, the arrival time, the positive phase duration, and the exponential decay coefficient for both the incident pressure and the reflected pressure [32]. Figure 3.7 shows a typical pressure history for the blast wave from the CONWEP model [32]. The total pressure on a surface due to a blast wave is a function of the incident pressure, reflected pressure, and the angle of the incident. The total pressure for $\cos\theta \geq 0$ is then given in Equation 3.3, and the total pressure for $\cos\theta < 0$ is shown in Equation 3.4 [32].

$$P(t) = P_{incident}(t)[1 + cos\theta - 2cos^2\theta] + P_{reflect}(t)cos^2\theta \tag{3.3}$$

$$P(t) = P_{incident}(t) \tag{3.4}$$

Eurocode 1 part 7 (EC 1-7) on accidental actions covers the calculations from gas explosions in road and rail tunnels. For this purpose, EC 1-7 provides empirical equations that can be used. These equations are given in Appendix A1 and are illustrated in Figure 3.9.

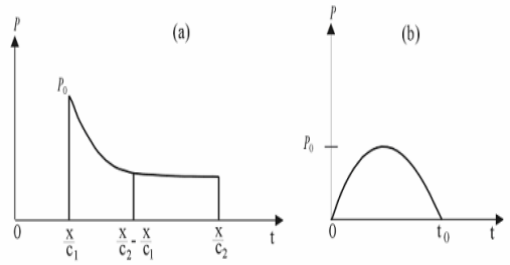

Figure 3.9: Pressure due to deflagration in tunnels [6].

3.2.7.2 Semi-Empirical Method

Semi-empirical methods rely on empirical approaches, consider simplified geometric factors, and may incorporate multiple reflecting surfaces. However, these methods are typically limited as they have been primarily developed for use by defense-related agencies [33].

3.2.7.3 Numerical Method

Numerical methods are mathematical techniques to solve complex problems that cannot be solved analytically [34]. These use computer programs to perform calculations and simulations, making it possible to obtain accurate and reliable results for problems that are too difficult or time-consuming to solve using traditional analytical, considerate element analysis. The key steps in applying numerical methods can be summarized as follows:

- Modelling the geometry of the structure
- Modelling the materials and sections by mesh
- Modelling the material properties of the structure, like contact formulations, constraints, and boundary conditions

The finished product may be a big and complex model, using a very fine mesh to obtain the outcome with as much accuracy as possible, which results in a large amount of data. Post-processing such huge data can be time-consuming and impossible on a small machine.

3.3 Material behaviour

This section focuses on the materials used in the SFTB, namely concrete and steel reinforcement. Understanding the behavior of these materials under various loading conditions and their response to elevated temperatures is crucial. Additionally, the numerical concrete model employed in this thesis will be introduced in detail. By investigating the material properties and incorporating accurate numerical models, a comprehensive understanding of the structural response of the SFTB can be achieved.

3.3.1 Concrete

Concrete is a composite material mainly consisting of Portland cement, water, and aggregates. The concrete is bonded together by the cement paste, i.e., cement and water. It can also contain various admixtures, depending on the wanted properties. The concrete typically changes from liquid to solid around 2 hours after pouring [35]. After that, the concrete continues to gain strength. Figure 3.10b shows a typical strength development curve. To achieve strong concrete a low water-to-cement (w/c) ratio is required. W/c ratio is the concrete's weight of water compared to its weight of cement [35]. If the concrete has a high w/c ratio, it can result in more porous concrete because there will be more spacing between the cement particles. Figure 3.10a illustrates the relationship between compressive strength and w/c ratio.

Regarding engineering design, the compressive strength of the concrete is the most important property. The typical strength range for concrete may be from C20/25 to C45/55, where 20 and 45 refer to the minimum required cylindrical compressive strength measured in mega-pascal (MPa) after 28 days, while 25 and 55 refer to the minimum required cubical compressive strength, also measured in MPa [33].

Typically, the strength of concrete is denoted by its compressive strength after 28 days. The concrete's strength depends on its curing time, as shown in Figure 3.10b. The graph indicates that concrete strength experiences the most significant increase in the initial

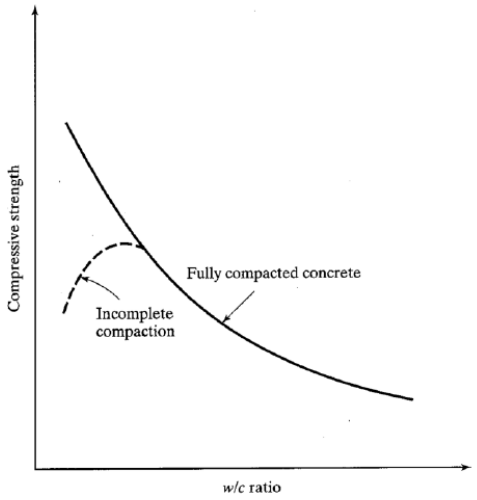

(a) The relationship between compressive strength and w/c ratio [36].

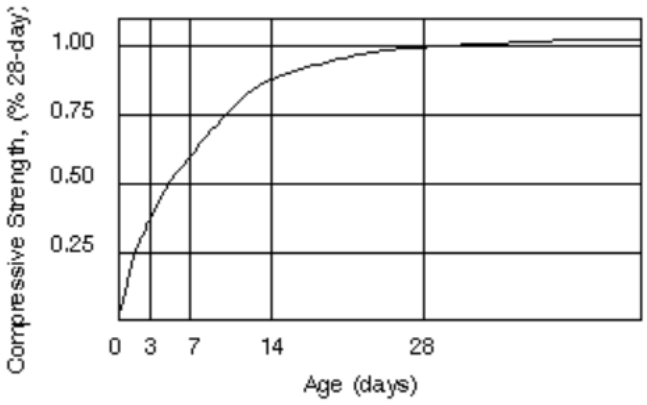

(b) A typical strength-gain curve [35].

Figure 3.10: Compressive strength of concrete

stages. The curing conditions are also essential to get maximum strength development. If the concrete is kept moist during the curing time, it will reach approximately 90% of its strength after 28 days [33]. The potential strength will be significantly reduced if the concrete dries out or freezes during this period.

Concrete is strong in compression but weak in tension. Typically, the tensile strength of concrete is only around 10% of its compressive strength, which is why concrete is rarely used without steel reinforcement. When subjected to high tensile forces caused by blast loads, the concrete may crack, resulting in superficial or deep fissures within the target material. If the cracks extend through the target's thickness to a significant degree, they can merge, causing fragmentation [33].

3.3.1.1 Numerical Concrete Model

There are several concrete models in LS-DYNA, including the concrete model 159 CSCM. The concrete model 159 is mainly used to analyze dynamic loading for RC structures and has been progressively developed since 1990 [37]. The concrete model 159 has one test-based model, (*MAT_159_CSCM (CSCM)), and one default model, (*MAT_159_CSCM_CONCRETE (CSCM concrete)), and is a type of cap model that combines a failure surface and a hardening cap in a smooth continuous way. For example, the yield surface in the meridional plane is shown in Figure 3.11 and uses a multiplicative formulation to combine the two surfaces [37]. This smooth intersection eliminates the need to deal with the numerical complexity of a compressive "corner" region between the failure surface and the cap. This model type is known as a smooth cap model or continuous surface cap model (CSCM) [37].

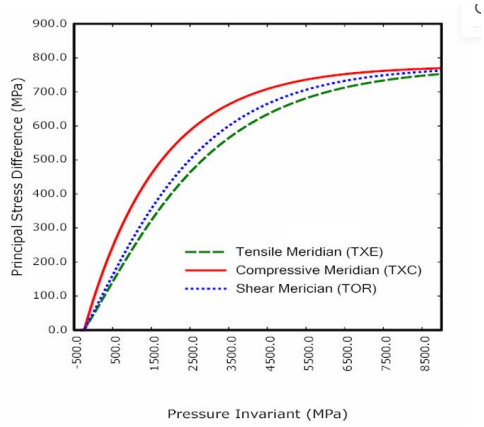

(a) Example plots of the failure surface in the meridional plane [37].

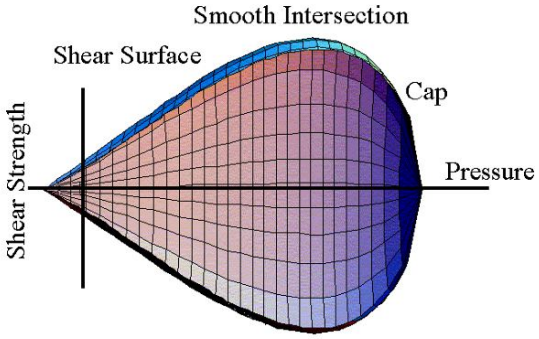

(b) General shape of the concrete model yield surface in two dimensions in the meridional plane [37].

Figure 3.11: Concrete model 159 yield surface

Concrete is a material that becomes weaker when subjected to tension or low to moderate compression [37]. This weakening, or "softening," is modeled using a damage formulation. If this damage formulation is not included, the model would predict a perfectly plastic behavior for test simulations, which is not realistic [37]. The damage formulation accounts for strain softening and modulus reduction, where strain softening decreases strength after reaching a peak value, and modulus reduction is a decrease in unloading/loading slopes

[37]. The damage formulation is represented by Equation 3.5.

$$\sigma_{ij}^{d} = (1 - d)\sigma_{ij}^{vp} \tag{3.5}$$

Where d is a scalar damage parameter that transforms the viscoplastic stress tensor without damage (σ^{vp}) into the stress tensor with damaged (σ^{d}) for this concrete model, brittle damage accumulates when the pressure is tensile. On the other hand, ductile damage gets when the pressure is compressive [37].

The behavior of the material in the concrete 159 model is described in a passive form to account for strain rate sensitivity [37]. This is important because the material's response can vary depending on how quickly it is deformed. The model incorporates a mathematical formula that considers both the elastic and plastic behavior of the material (see Equation 3.6 and 3.7) [37]. It also considers a user-defined parameter known as the fluidity coefficient, which represents the material's response to changes in strain rate. By adjusting this coefficient, the extent of plastic deformation and the material's behavior at different rates can be controlled. This formulation enables accurate simulation and understanding of concrete structures under various loading conditions, particularly when high strain rates are involved [37].

$$\sigma_{ij}^{vp} = (1 - \gamma)\sigma_{ij}^{T} + \gamma\sigma_{ij}^{p} \tag{3.6}$$

$$\gamma = \frac{\Delta t/\eta}{1 + \Delta t/\eta} \tag{3.7}$$

Where:

σ_{ij}^{vp} = Viscoplastic stress tensor

σ_{ij}^{T} = Trial elastic stress tensor

σ_{ij}^{p} = The plastic stress tensor

η = The fluidity coefficient

Δt = The timestep

3.3.2 Fire Response of Concrete

Concrete structures may be exposed to fire during their service life, leading to economic and social damages. Concrete is very fire resistant and is the preferred construction material in fire-susceptible constructions [38]. However, at high temperatures, the concrete undergoes severe spalling. The phenomena of spalling involve the ejection of chunks of concrete for the material's surface due to the reduction in the surface tensile strength [39]. Mechanical forces are gathered within the concrete due to rapid heating, in other words by thermal stresses and by the sudden expansion of the moisture in the pores within the structure [39].

The water within the concrete begins to vaporize at temperatures from 100°C and up. When the water starts to evaporate, it is usually causing a build-up of pressure in the concrete [39]. Due to the pressure effect, the boiling temperature tends to range between 100°C to 140°C [39]. When the temperature reaches around 400°C, the calcium hydroxide will start to dehydrate, generate more vapor, and significantly reduce the physical strength of the concrete. As the temperature increases, there will occur other changes in the aggregates. For example, 575°C, the quartz-based aggregates will expand because of a mineral transformation, while limestone will start to decompose at a temperature of 800°C [39]. The thermal response of the aggregates itself is one thing, but how it can affect the concrete is another, as they may have different expansion rates and can lead to cracks and spalling of the concrete. The combination of physical and chemical changes in the concrete will reduce the material's compressive strength. If the concrete is exposed to temperatures beyond 350°C, the strength drops rapidly, and by 600°C the concrete can be expected to have lost 55% of its ambient strength [40].

3.3.3 Fire Response of Steel Reinforcement

During a fire, the performance of steel reinforcement is better understood than concrete, and predicting the strength of the steel can be done with reasonable confidence [39]. Steel types with low carbon content tend to exhibit "blue brittleness" when exposed to temperatures between 200-300°C [39]. Concrete and steel expand similarly at temperatures up to 400°C; however, steel will expand significantly at very high temperatures compared to concrete. If the temperatures reach 700°C or more, the load-bearing capacity of the

steel reinforcement will be reduced to approximately 20% of its design strength [39].

The steel reinforcement may also have a significant effect on the transport of water in the heated concrete. It creates a barrier that may trap the water and leads it around the reinforcement bars. This may lead to increased pore pressure and potentially spalling of the concrete. However, the water gathered around the reinforcement bars can also reduce the temperature in the concrete [39].

3.4 Numerical Analysis

The thesis relies on the utilization of a non-linear finite element analysis in a finite element model. Therefore, having a thorough understanding of the theory behind the finite element method is crucial. Non-linear finite element analysis represents an advanced approach in structural analysis, considering multiple sources of non-linearity, including geometry, material properties, and boundary conditions.

3.4.1 Finite Element Method

The Finite Element Method (FEM), also known as Finite Element Analysis (FEA), is utilized for solving field problems through numerical techniques. In a field problem, the spatial distribution of one or more dependent variables is sought, which is mathematically described by differential equations or integrals expressed as matrices [34]. In FEM, the structure is partitioned into small elements, where each element represents a portion of the structure with a simple spatial variation of the field quantity. These elements are interconnected at nodes to form a mesh [34]. Several advantages are offered by FEM, including the applicability to various field problems such as heat transfer and magnetic fields, the capability to analyze bodies of any shape, the flexibility in applying boundary conditions to specific regions of the structure, and the ability to handle material properties that may vary from one element to another, without being constrained by isotropy [34].

3.4.2 Explicit method

Both implicit and explicit solvers may be used to solve the general equation system of the equation of motion (see Equation 3.8).

$$M\ddot{u}(t) + C\dot{u}(t) + Ku(t) = R^{ext}(t) \tag{3.8}$$

Where u is the nodal displacement vector, and M, C, and K are the mass, damping, and stiffness matrices, respectively. R^{ext} is the external force vector.

Explicit solvers are more attractive for dynamic analysis, which usually contains large equation systems, as the solution scheme does not require matrix inversion or interactions [41]. Moreover, explicit solvers are much more computational for solving one-time step than solvers based on the implicit scheme. However, the explicit method is only stable if the time step size is sufficiently small, while the implicit system is unconditionally stable for significant time steps [41]. This makes explicit solvers a good alternative for shorter-time transients such as blast response or instance impact. The equations for time step control for beam elements (Equation 3.9) and solid elements (Equation 3.10) are described below [42].

$$\Delta t_e = \frac{L}{c} \tag{3.9}$$

Where:

Δt_e = The critical time step size

L = The length of the element

c = The speed of sound

$$\Delta t_e = \frac{V_e}{cA_{e,max}} \tag{3.10}$$

Where:

Δt_e = The critical time step size

V_e = The element volume

$A_{e,max}$ = The area of the largest side

c = The speed of sound

3.4.3 LS-DYNA

This thesis is based on an FE model created in LS-DYNA Prepost. LS-Prepost is a part of the LS-DYNA product and is an advanced pre- and post-processor tool. This tool is used to create the FE model and analyze the simulation results. The FE models of complex structures can be advanced and time-consuming regarding simulation time. Therefore it is crucial to get correct results. Moreover, if the user of LS-DYNA or any other FE program lacks knowledge of FEA, it can lead to severe consequences [34].

4 Preliminary Simulations

This chapter presents the preliminary simulations conducted to explore the behavior of the proposed design and validate the numerical material and blast models used. The simulations involved utilizing the finite element analysis software LS-DYNA. The purpose of these simulations was to investigate the performance of the proposed material and blast models under blast loading and compressive loads, with the goal of identifying any potential design issues or limitations.

4.1 Numerical Setup

This section provides a concise overview of the numerical setup employed for the material and blast models proposed for this thesis.

4.1.1 Concrete

The concrete model 159 has one test-based model, (*MAT_159_CSCM (CSCM)), and one default model, (*MAT_159_CSCM_CONCRETE (CSCM concrete)), as mentioned in Section 3.3.1.1. The material model CSCM has adjustable parameters that can be calibrated based on standard material tests like cube compressing, cylinder compression, and tensile splitting, requiring no less than 49 input parameters. This means that the user of CSCM is required to define the material parameters based on experimental testing, which allows for a more accurate simulation of the material's response. However, since CSCM can provide more accurate and detailed modeling results, the cost of computational effort and complexity in defining the material parameters will increase severely. Unlike the CSCM, the CSCM concrete has built-in parameters that do not require the user to determine the material parameters based on experimental data. However, 12 parameter inputs are still necessary to specify the strength class of the desired concrete, as indicated in Table 4.1. The built-in parameters provide good results for quasi-static engineering stress-strain curves obtained from cylinder compressive strength of the concrete, but it underestimates the tensile strength [43]. Therefore, to simplify the modeling process and reduce the computational time required to define the material properties and behavior, CSCM concrete is utilized in the numerical modeling for this thesis.

Table 4.1: Parameter inputs for CSCM concrete corresponding to B45 concrete

Properties	**Value**
RO (Density, kg/m^3)	2400
NPLOT (Plotting option)	7 (Plastic volume strain)
INCRE (Max strain increment)	Default
IRATE (Rate effect option)	1 (on)
ERODE (Element erode time)	1.1
RECOV (Compression recovering)	Default
ITRETRC (Cap retraction option)	0 (Cap does not react)
PRED (Pre-existing damage)	0
FPC (Compressive strength, MPa)	45
DAGG (Max aggregate size, m)	0.022
UNITS (Units option)	Pa, m, sec, kg/m^3,N

4.1.2 Blast

There are several solution strategies for blast loading in LS-DYNA. For this thesis, the *LOAD_BLAST_ENHANCED is utilized (keyword file can be found in Appendix A2). This model is derived from the blast loading equations outlined in UFC 3 340 02 ([2]) and CONWEP (as discussed earlier in Section 3.2.7.1), which are primarily based on the experimental data collected by Kingery and Bulmash (Section 3.2.7.1) concerning the free air blast from spherical and hemispherical surface charges of TNT [44]. The modified Friedlander equation represents the pressure-time history P(t) of the reflected pressure (see Equation 4.1) [11]. The modified equation is more accurate than the original equation because it also includes the negative phase of the incident pressure (illustrated as the yellow area in Figure 3.6). However, this thesis does not include the negative phase in the paramedic study or the SFTB model because its effects are considered minor for cases of internal blast loading [11].

$$P_s(t) = P_{S0}(1 - \frac{t - t_A}{t^+})e^{-b\frac{t-t_A}{t^+}} \tag{4.1}$$

Where:

P_{S0} = The peak overpressure

t_0 = The positive phase duration

b = The decay coefficient of the waveform

t = The time elapsed, measured from the instant of blast arrival

The SFTB model is big and has a massive computational cost because of the fine mesh. While the *LOAD_BLAST_ENHANCED on the other hand, is an engineering model requiring minimal input and minimal CPU requirements, which can help to reduce the simulation time compared with for example, Particle Blast or Smooth Particle Blast [44]. These blast models are also called "first principle" models and require extensive user input, resulting in substantial computing resources [44]. *LOAD_BLAST_ENHANCED was selected as the blast model for this thesis due to its computational efficiency, which enables efficient simulation of the target response of interest. This model also provides a valuable tool for target model debugging and insights into the expected structural response when more complex "first-principle" methods are subsequently utilized [44].

4.1.3 Mesh

Choosing the appropriate mesh size is crucial for obtaining accurate and reliable results in numerical simulations. The mesh size affects the accuracy and efficiency of the simulation. If the mesh size is too coarse, the results may be inaccurate or unreliable, as the model may not capture the details and complexities of the simulated physical system.

In numerical analysis, the mesh size determines the number of elements used to discretize the model's geometry and the extent of the problem being solved [44]. A finer mesh results in more elements and a more significant problem size, which increases the computational cost and time required to solve the problem. This can be a problem for large-scale simulations, where the computation time can become prohibitive if the mesh is too fine. Therefore, choosing a mesh size involves balancing the need for accuracy and computational efficiency.

4.2 Parametric Study

In engineering and science, parametric studies are commonly used to optimize the design of the structure, material, and processes. In this case, the parametric study is done on small-scaled models to calibrate and assess the numerical material and blast model before proceeding to the more complex structure involving blast loads.

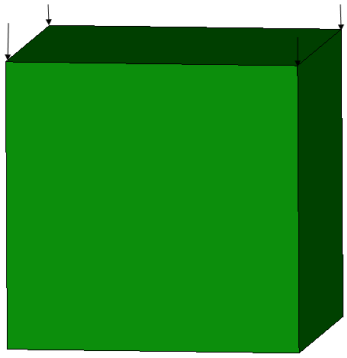

Figure 4.1: The cube subjected to -12.5 MPa in each top node.

4.2.1 Compression Test

Similar to a uniaxial compression test performed in a laboratory, the numerical uniaxial test is used to determine the compressive strength of the chosen material model. Performing tests on the selected material model is essential to investigate if the material model would capture the behavior as expected for the material. In the test, a cube sample of CSCM concrete, or one mesh, with dimensions 100x100x100 mm was subjected to -12.5 MPa in each node, a total of -50 MPa, while the bottom was restrained in the y-direction (see Figure 4.1). The compressive strength of the concrete is determined by measuring the maximum load the cube can withstand before yielding. The result from the numerical compression test was used to calibrate the material model, ensuring that it represents the behavior of the real material.

4.2.1.1 Mesh Size

To evaluate the response and behavior of the MAT 159 CSCM material model, a compressive test is performed using only one numerical element, or mesh. This approach is chosen to test the maximum strength of the material, rather than its deformation behavior. Since the CSCM model incorporates a smooth intersection between the failure surface and the hardening cap, a single-element compressive test can accurately measure the maximum strength of the material without the need for multiple elements to capture damage initiation and propagation. While this method does not provide information on the deformation behavior of the material, it is a useful approach to evaluate the strength properties of the material model. The lack of visible damage in the single-element test also eliminates any potential complications that may arise from damage accumulation and

propagation, allowing for a more straightforward evaluation of the material's maximum strength.

4.2.1.2 Results

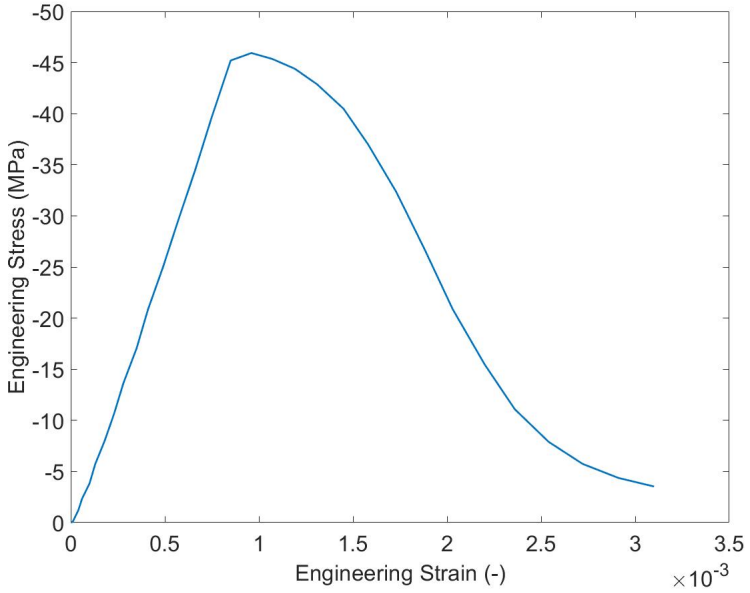

Figure 4.2: Overview of the uniaxial compression test, where the results are in terms of engineering strain (x-axis) and engineering stress (y-axis).

The CSCM concrete was given the properties of B45 concrete, which, as per Eurocode 2, is expected to endure a compressive load of 45 MPa (f_c) [6]. The test did not take into account friction, because it was conducted by only using one CSCM concrete element and no load plates. This means that there was no friction between the load and the test specimen. If load plates had been used, it is possible that the test results would have shown slight variations.

The obtained compressive engineering stress and strain are illustrated in Figure 4.2, clearly demonstrating that the CSCM concrete cube withstood the uniaxial compression test. The engineering strain was calculated using Equation 4.2, while the engineering stress was determined using Equation 4.3. Based on this result, it can be concluded that the concrete model is adequate for utilization in the SFTB model.

$$\epsilon = \frac{L - L_0}{L0} \tag{4.2}$$

$$\sigma = F/A_0 \tag{4.3}$$

4.2.2 Blast Test

This preliminary study aimed to assess the accuracy and suitability of the blast model for the main model of the SFTB. To achieve this, a calibration model consisting of a half-symmetric pipe with an internal diameter of 200 mm (illustrated in Figure 4.3) was used. The blast load simulation results were validated by comparing them with the experimental investigation carried out by Kristoffersen et al. ([7]) on the same pipe (as discussed in Chapter 2). This comparison aimed to determine whether *LOAD_BLAST_ENHANCED in the blast simulation produced similar damage to the pipe as the C-4 detonation did in the experimental study. These results will highlight any inconsistencies and limitations of the numerical model, which can be avoided in the main model.

4.2.2.1 Geometry

It is essential to emphasize that the pipe used in this study should not be regarded as a small-scaled SFTB but rather as a concrete pipe. The selection of this specific geometry is based on its tubular shape, which allows for the examination of how the blast model behaves as an internal explosion, similar to its behavior in the main model. The geometric characteristics of the pipe are illustrated in Figure 4.3. The total length of the pipe is 1,560 mm, with a wall thickness of 41 mm. The internal radius is 200 mm, and its ends are constrained in all directions.

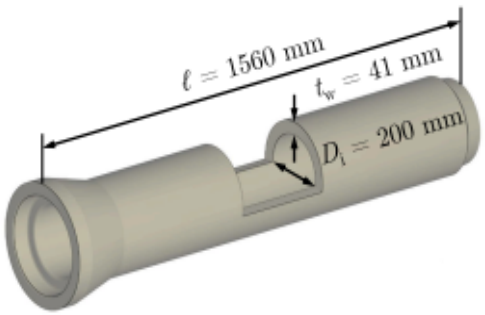

Figure 4.3: Geometry of the concrete pipe. Credit: Kristoffersen et al. [7].

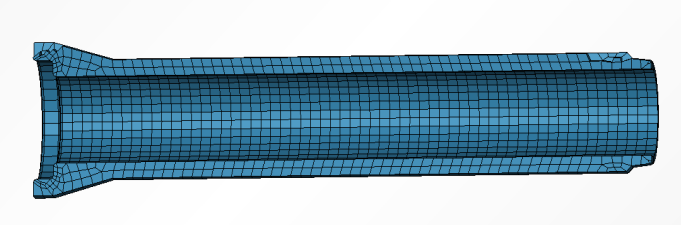

Figure 4.4: Mesh for the pipe.

4.2.2.2 Mesh

The mesh used in this study is illustrated in Figure 4.4 and consisted of 4800 elements with a size of 25x25 mm and 7008 nodes. While a finer mesh may have been preferred for a more detailed simulation of the concrete structure, this study aimed to investigate the accuracy of the blast model rather than the concrete structure itself. Therefore, this mesh was considered sufficient for replicating the key experimental results reported by Kristoffersen et al.

4.2.2.3 Detonation

The numerical model utilized a charge size of 30 grams TNT, while the experimental testing employed a charge size of 25 grams C-4. The charge was positioned at the center of the pipe, as depicted in Figure 4.5. To determine the TNT-equivalent charge, the following calculation was employed (TNT-equivalency is discussed in detail in Section 3.2.1.1):

$$W = (\frac{4.715}{4.184}) \times 25g = 28.17grams \simeq 30grams \tag{4.4}$$

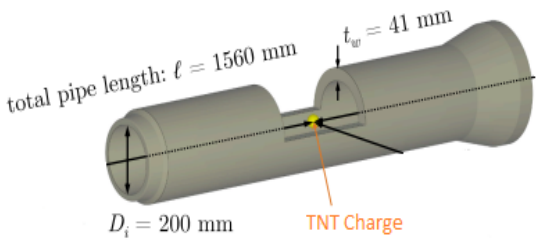

Figure 4.5: Charge position. Credit: Kristoffersen et al. [7].

4.2.2.4 Results

The numerical testing conducted on the pipe gave good qualitative results. The damage pattern observed in the experimental study, shown in Figure 4.6, indicates that the middle portion of the pipe sustained the most damage while the ends remained unscathed.

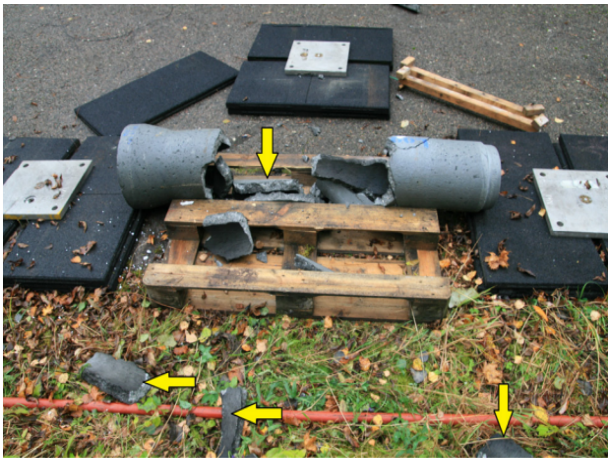

Figure 4.6: Pipe after testing a detonation of 25 g C-4 charge. Credit: Kristoffersen et al. [7].

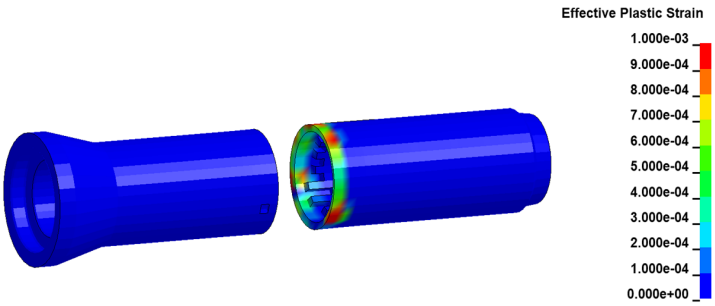

Figure 4.7: Contour plot of the effective plastic volumetric strain after numerical testing a charge size of 30 g TNT.

Similarly, the damage pattern observed in the numerical model, as shown in Figure 4.7, also reveals that the middle portion of the pipe sustained the most damage. However, to reproduce the exact extent of damage observed in the experiment, a higher charge size of TNT would be required for the numerical model. A possible explanation for this is the slight under-prediction of the blast load by the blast model. Additionally, it should be noted that the low values of Z (scaled distance in Equation 3.2) may introduce inaccuracies in the analysis.

The concluding remarks for the blast model are that this blast model is a good alternative for a first approach of blast simulation and testing, which does not include investigating the structure fragments or crack development during and after the explosion. For more detailed testing, a more advanced blast model should be utilized. However, *LOAD_BLAST_ENHANCED is sufficient for the SFTB model because the main focus is the overall damage and impact on the internal structures.

5 Numerical Model of Intact SFTB

This chapter presents an in-depth analysis of the dynamic response of secondary constructions in SFTBs under blast loading conditions, utilizing numerical simulations. The primary objective of these simulations is to investigate and evaluate the behavior and performance of the secondary structures when subjected to blast loading. The simulations are conducted in two stages: first, by subjecting the internal constructions to blast loading and focusing solely on the behavior of the concrete material, and second, by considering the internal constructions as reinforced concrete structures exposed to the highest charge size of TNT. The reason for conducting the simulations in two stages was to assess the extent of damage caused by different charge sizes and then investigate the ones that caused the most significant damage to the internal structures.

5.1 Numerical Setup

This section provides an introduction to the numerical setup of the SFTB model, which encompasses the geometry, mesh, material models, and blast location.

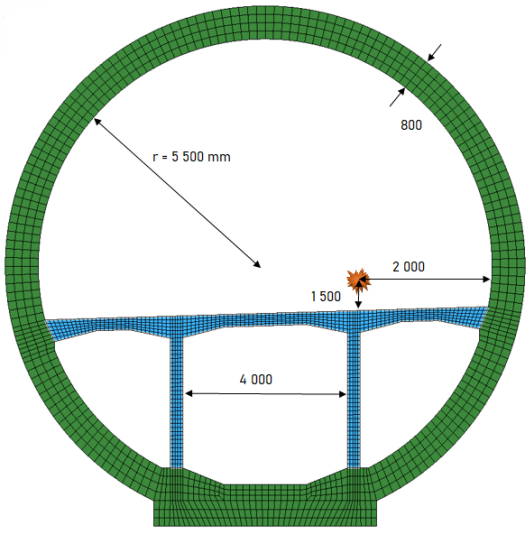

Figure 5.1: Geometry and mesh for the SFTB profile. Measures in millimeters (mm).

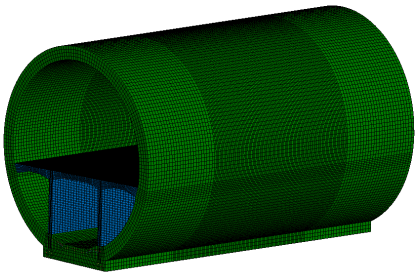

(a) Geometry and mesh for external construction.

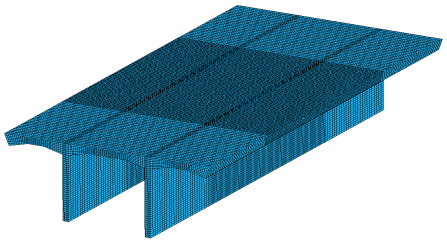

(b) Geometry and mesh for the internal constructions.

Figure 5.2: Geometry and mesh for the external and internal SFTB.

5.1.1 Geometry and Mesh

Several cross sections have been proposed for SFTB, including rectangular and circular designs. For this thesis, the model is based on technical drawings from NPRA's feasibility study for crossing the Sognefjord (see Appendix B). As depicted in Figure 5.1, the model consists of a circular concrete frame with a thickness of 800 mm and internal components, including a concrete deck ranging from 500 to 200 mm thick and concrete load bearing walls with a uniform thickness of 300 mm. With a span of 20 m, the blast location was positioned 10 m from the tunnel opening, making the central part of the tunnel particularly susceptible to blast-induced damage.

The accuracy and reliability of the simulation results are of utmost importance, and they heavily rely on the quality of the mesh used in the model. In this study, significant effort was dedicated to optimizing the mesh design, aiming to strike a balance between capturing intricate details and complexities while maintaining computational efficiency. Specifically, a meticulous approach was employed to ensure that each component of the construction had a sufficient number of elements through the thickness of the cross section, with a minimum of four elements. The mesh used in the simulation followed a deliberate strategy, featuring a finer resolution in the central region (as illustrated in Figure 5.3), where higher accuracy was deemed critical. In contrast, a coarser resolution was employed in the outer parts to improve computational efficiency. This mesh design strategy is clearly illustrated in Figure 5.2, where the variation in element size is evident.

Although the model employed 686,385 elements and 740,071 nodes, it is essential to note that an even finer mesh would have been desirable to achieve more precise results. However,

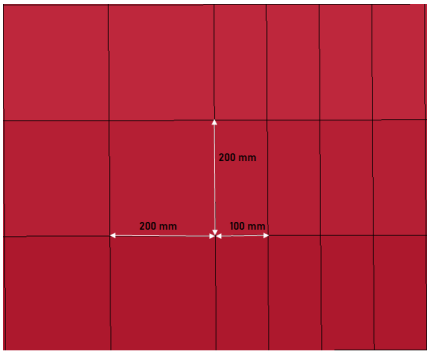

Figure 5.3: Element size of the inner (100x200 mm) and outer (200x200 mm) parts of the model.

considering the model's size, implementing such a fine mesh would have significantly increased the computational time, rendering the simulation impractical to run within reasonable time constraints. Hence, striking the right balance between accuracy and efficiency was crucial when designing the mesh for such a large-scale model.

5.1.2 Material Setup

The material model selected for the SFTB was the CSCM concrete, which was tested in the preliminary study (Chapter 4). Following the evaluation of the material model's response to compressive stress and blast loading in the preliminary study, it was determined that CSCM concrete was appropriate for the SFTB model. As previously discussed in Chapter 4, the CSCM concrete necessitates 11 input parameters for defining its behavior. These parameter inputs are presented in Table 4.1, corresponding to B45 concrete.

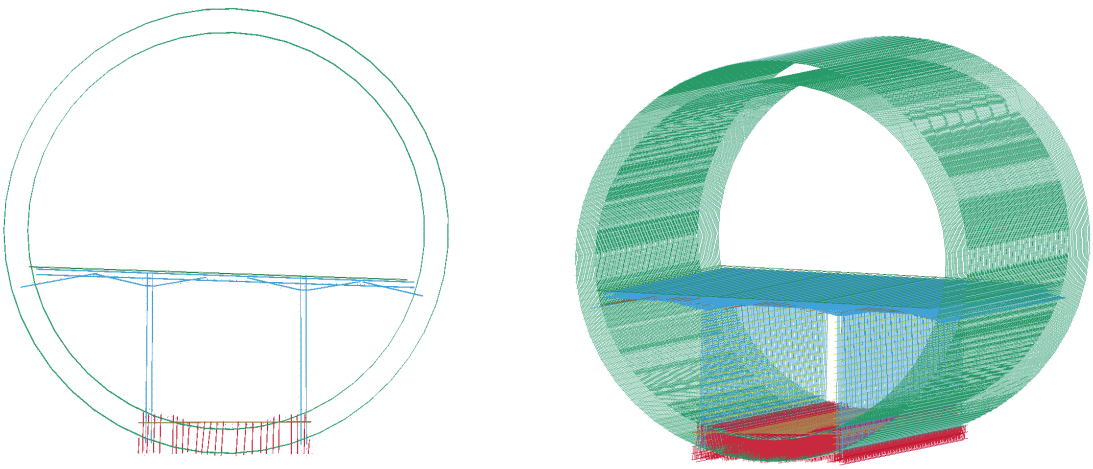

Figure 5.4: Reinforcement illustrated in profile (left) and from the side (right).

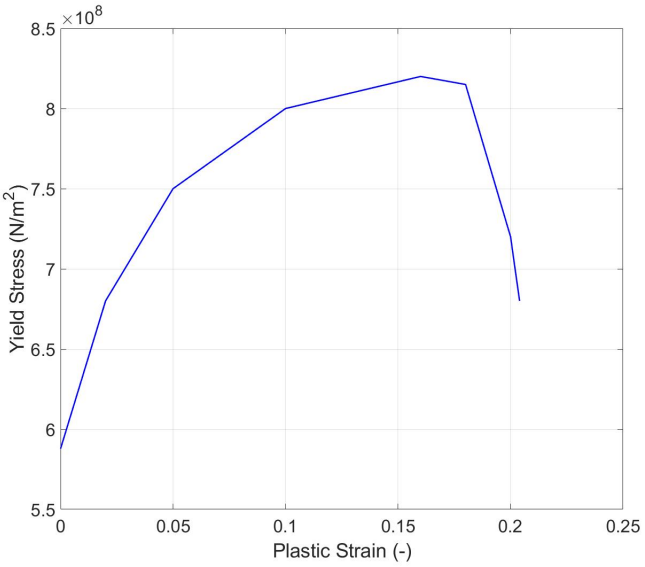

Figure 5.5: Yield stress and plastic strain curve.

The technical drawings provided by NPRA, which are available in Appendix B, incorporated different sizes of bar reinforcement. For this thesis, three specific sizes were adopted: 16 mm, 20 mm, and 36 mm. In the numerical model (illustrated in Figure 5.4), the steel reinforcement is represented as bar elements in LS-Prepost and is assigned material properties using the *MAT_024_PIECEWISE_LINEAR_PLASTICITY (MAT024) material model. MAT024 requires 29 parameters to define the properties of the steel reinforcement, which are listed in Table 5.1. Additionally, the parameters governing the strength development curve should also be included in Table 5.1, but are instead illustrated in Figure 5.5.

MAT024 is an elasto-plastic material model that defines arbitrary stress versus strain curve and arbitrary strain rate dependency. Furthermore, failure based on the plastic strain or a minimum time step can be defined [45].

The reinforcement was assigned a 50 mm concrete cover from the inner and outer surfaces to provide sufficient protection. The model consisted of 686,385 elements, of which 394,635 were beam elements with an element size of 100 mm. Like the solid elements, the beam elements were subdivided into smaller ones to represent the deformation profile accurately.

To accurately simulate the behavior of RC, it was necessary to establish a connection between the solid and beam elements. This was accomplished by utilizing the *CONSTRAINED_BEAM_IN_SOLID keyword, which enabled a constraint-based

Table 5.1: Parameter inputs for MAT024

Properties	**Value**
RO (Density, kg/m^3)	7800
E (Youngs modulus, N/m^2)	2.00e+11
PR (Poisson's ratio)	0.3
SIGY (Yield stress, N/m^2)	5.88e+08
ETAN (tengent modulus)	0 (Ignored)
FAIL (Failure flag)	0.25
TDEL (Minimum element deletation time step)	0
C (Strain rate parameter)	0
P (Strain rate parameter)	0

coupling between the two element types. In this coupling, the beam elements were constrained to move in conjunction with the solid Lagrangian elements, which was serving as the master component. This approach ensured the cohesive interaction between the different components of the RC structure and allowed for a more realistic representation of its behavior under dynamic loading conditions [46]. The initial simulations focused solely on the concrete response and were performed without employing the *CONSTRAINED_BEAM_IN_SOLID keyword. These simulations served to examine the structural behavior of the concrete material. Subsequently, a simulation was conducted using a charge size of 200 kg to model the RC structure, incorporating the interaction between the solid and beam elements.

The *MAT_ADD_EROSION material model simulates fracture propagation in a mesh-based system. This model depends on the mesh and is often utilized to visualize the extent of the damage. When a material element in the model is significantly damaged and reaches its critical value, the model removes it from the FE model. This process allows for a dynamic representation of the fracture propagation and provides insights into the damage progression of the material.

5.1.3 Boundary Conditions

In contrast to the pipe from the preliminary study, the SFTB is only restricted along its longitudinal direction (in this case, the z-axis). This allows the nodes to move more freely in the plane, which provides the user with a more accurate capture of the model's behavior under blast loading.

5.1.4 Blast Setup

In the preliminary study, the blast model *LOAD_BLAST_ENHANCED was also examined. Based on qualitative results, it was determined that the blast model was adequate for the full-scale SFTB model. The main objective of this thesis is to investigate the blast response of the secondary structures and assess the damage resulting from blast loading. In this context, the *LOAD_BLAST_ENHANCED model is suitable since the focus is on overall damage rather than crack development or fragment analysis. However, it is essential to note that a more advanced blast model would be required if the objective were to obtain more detailed information about crack development or fragments.

To understand the damage to the internal constructions, tests were conducted using three TNT charge sizes: 100 kg, 150 kg, and 200 kg. All charge sizes were positioned in the exact location as illustrated in Figure 5.1.

5.1.5 Energy Balance

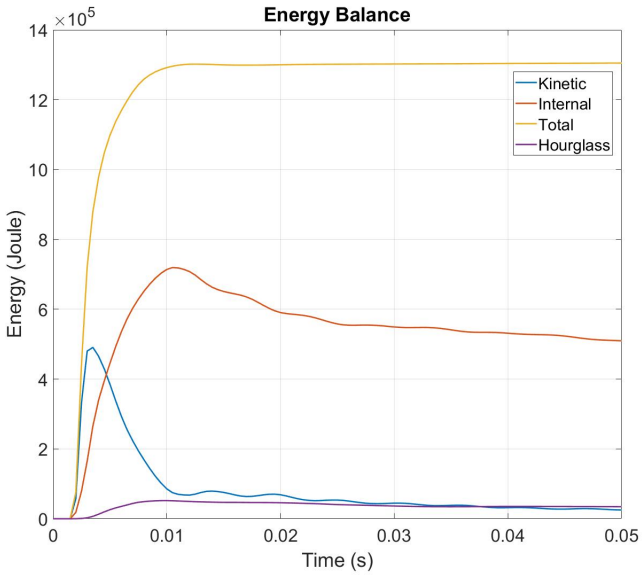

Figure 5.6: The development of total-, internal-, kinetic- and hourglass energy.

Before analyzing the results, an energy balance check was conducted to ensure the simulations were executed as expected. This check involves examining the curves of total, kinetic, internal, and hourglass energy and the energy ratio. These checks serve as valuable tools for users to verify the accuracy of the simulations.

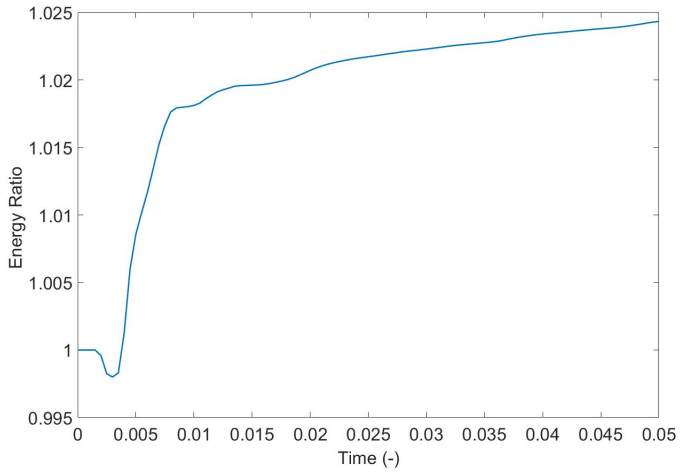

Figure 5.7: The energy ratio curve.

The hourglass energy, in particular, should not exceed 5% of the total energy, serving as a rule of thumb [47]. Figure 5.6 indicates that the hourglass energy accounts for approximately 3-4% of the total energy, well within the acceptable range. Additionally, the energy ratio should not exceed 1 with a deviation of more than +/- 0.05 [48]. Figure 5.7 demonstrates that the energy ratio remains within the acceptable range, further confirming the accuracy and reliability of the simulation results.

Kinetic energy represents the total energy processed by the TNT charge, while internal energy denotes the cumulative energy within the system, encompassing all types of energy processed by the system. The total energy is the sum of all energy components in the system. As illustrated in Figure 5.6 and Figure 5.7, the energy balance checks demonstrate a valid energy distribution for the unreinforced SFTB model exposed to a 200 kg charge. These checks were only performed for the 200 kg charge scenario, as the only difference among the models lies in the TNT charge utilized.

5.2 Results Without Reinforcement

The results of the full-scaled SFTB simulation revealed valuable insights into the effects of different charge sizes on the internal constructions of concrete. The simulations, executed on a high-performance computer (HPC) with 64 CPUs, required approximately two hours to complete.

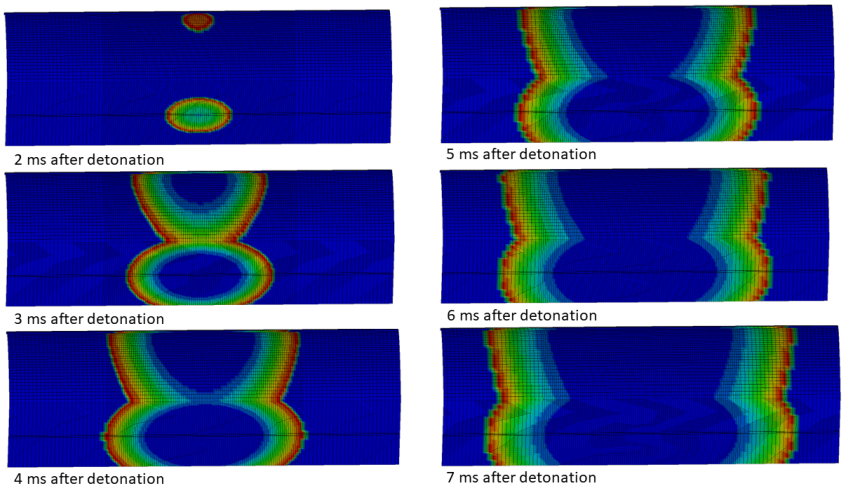

Figure 5.8: Contour plot of the incident pressure propagating through the SFTB after 2ms, 3ms, 4ms, 5ms, 6ms, and 7ms.

5.2.1 Blast Load Distribution

The blast load distribution of blast pressure is essential to analyze, to identify critical regions within the tunnel where stress concentrations or potential weaknesses may occur. Figure 5.8 illustrates the propagation of incident pressure (P_i) through the SFTB over a time period of 2-7 ms, originating from the location depicted in Figure 5.1 and spreading outward from the center of the model.

This distribution of blast pressure highlights areas within the internal constructions that experience the highest values of blast loading, which is critical for assessing the structural response.

5.2.2 Structural Response

Among the internal constructions analyzed in this model, particular attention is given to the deck as it experiences the highest exposure to the blast loading. As a result, the tunnel deck exhibits the most significant displacement, effective plastic volumetric strain, Von Mises stress, and element erosion. The most affected areas are at the sides of the load-bearing wall, beneath the explosion point, as depicted in Figure 5.9.

This thesis primary focus on the displacement in the y-direction resulting from high blast loading and pressure generated by the detonation. Figure 5.9 provides a visualization of the maximum displacement observed 7-8 ms after the detonation for the three charge

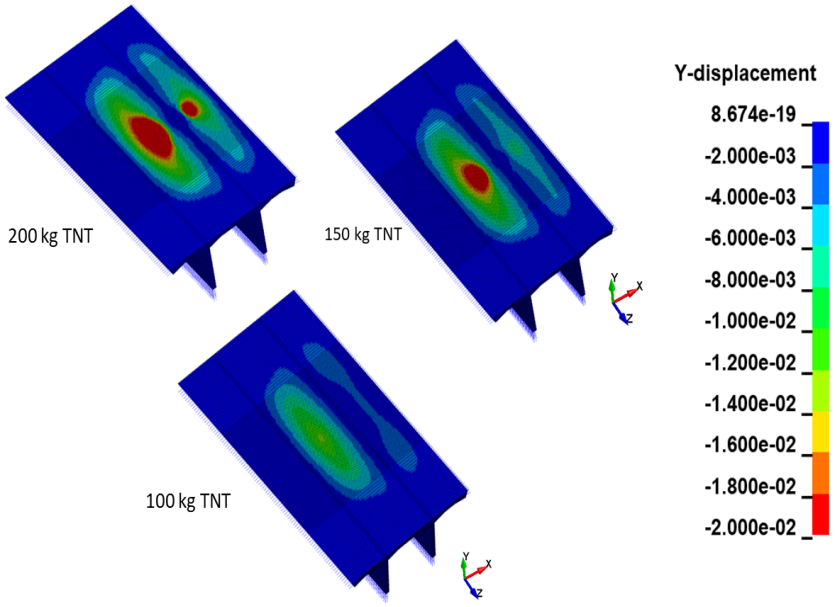

Figure 5.9: Contour plot of the displacement in y-direction after 7-8 ms.

sizes. Among these sizes, the 200 kg TNT charge exhibits the most significant overall displacement, measuring around 20 mm over a wide area. This displacement is notably larger in comparison to the 10-12 mm displacement observed on the deck exposed to a 100 kg TNT charge. Interestingly, no visible damage is observed on the top surface of the deck for all charge sizes.

After subjecting the SFTB to blast loading of different charge sizes, the nodal analysis provides insight into the structural response and deformation pattern. The nodal displacement reveals the magnitude and direction of movement experienced by each node in the SFTB. Figure 5.10 illustrates the maximum nodal displacement in the y-direction for all three charge sizes (see Appendix A2 for nodal location). This provides essential information on how the SFTB's deck responds to the varying blast intensities. For example, Figure 5.10 shows that increasing the charge size from 150 kg to 200 kg TNT makes a massive difference in the nodal displacement of the deck. The results are also indicating that the nodal displacement resulting from the 200 kg TNT goes from negative to positive direction. A possible explanation for this phenomenon could be that the blast load exerts a sudden and intense pressure on the structure. This pressure generates an initial impulse, causing the nodes in the structure to move in the opposite direction of the blast wave. Another explanation could be elastic rebound. As the blast wave passes through the model and "away from the structure," the forces acting on the nodes change

direction.

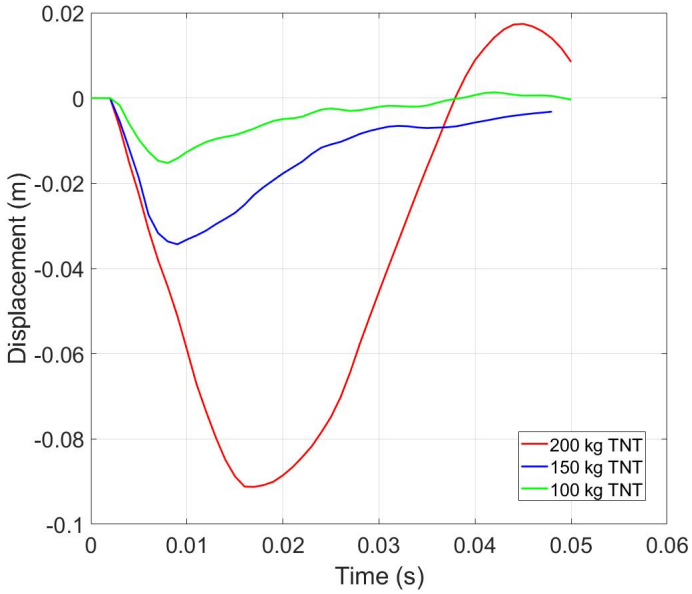

Figure 5.10: Nodal displacement in y-direction for all three charge sizes.

5.2.3 Stress and Strain Distribution

The significance of stress and strain distribution within the internal constructions of the SFTB is crucial for understanding the structural response. High stress and strain concentrations have essential implications for the tunnel structure's integrity, stability, and load-carrying capacity.

The analysis of effective plastic volumetric strain reveals areas within the internal constructions that have experienced significant deformation or elongation due to the blast loading. For example, in Figure 5.11a, it can be observed that the highest concentration of effective plastic volumetric strain occurs near the load-bearing wall and the center of the deck, which is directly beneath and beside the explosion location. This strain concentration can lead to structural weaknesses, such as cracking, delamination, or excessive displacements, potentially compromising the overall integrity of the tunnel.

Similarly, the analysis of Von Mises stress highlights areas where the applied forces and loads are concentrated. Figure 5.11b demonstrates the highest stress concentration near the load-bearing wall, particularly on the top surface of the deck, as indicated by the red areas that are most susceptible to yielding. Also, high stress concentrations are observed along the junction between the deck and the wall on the bottom surface. This could

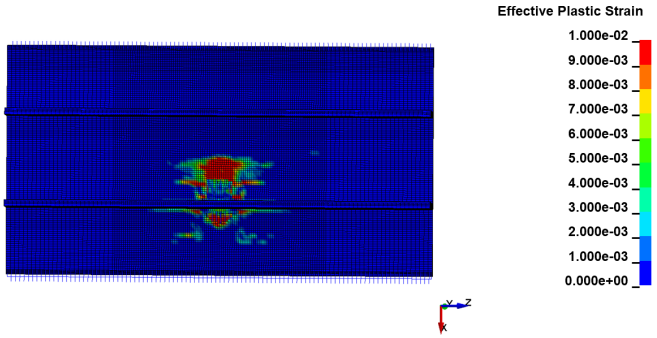

(a) Contour plot of the effective plastic volumetric strain at 41 ms after the detonation of 200 kg TNT.

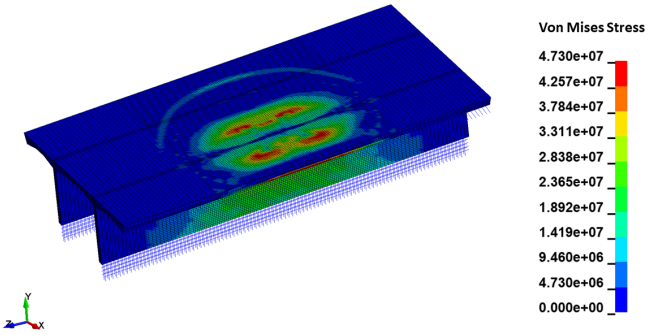

(b) Contour plot of the Von Mises stress at 4 ms after the detonation of 200 kg TNT.

Figure 5.11: Contour plot of the effective plastic volumetric strain and the Von Mises stress.

be attributed to the combined stress from the main tunnel construction and the deck, resulting in a higher stress concentration at that junction. Excessive stress concentrations can result in material yielding, buckling, or even fracture, further compromising the structural integrity.

5.2.4 Damage Assessment

Utilizing the element deletion feature (*MAT_ADD_EROSION) in LS-DYNA, the damage to the internal structures caused by the blast load can be effectively visualized, as demonstrated in Figure 5.12. The severity of the damage can be classified as moderate since the blast did not result in a fracture through the deck.

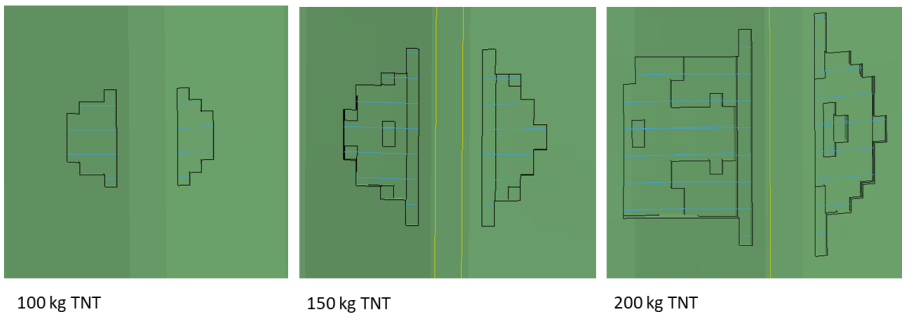

Figure 5.12: Removed elements due to MAT_ADD_EROSION.

5.2.5 Comparative Analysis

Figure 5.13 presents a contour plot of the effective plastic volumetric strain, showcasing the plastic deformation of the deck from its bottom surface. The results demonstrate a clear correlation between the charge size and the extent of plastic deformation. Notably, charge sizes of 100 kg and 150 kg exert minimal influence on the plastic deformation of the deck, whereas a charge size of 200 kg significantly impacts the bottom surface's plastic deformation.

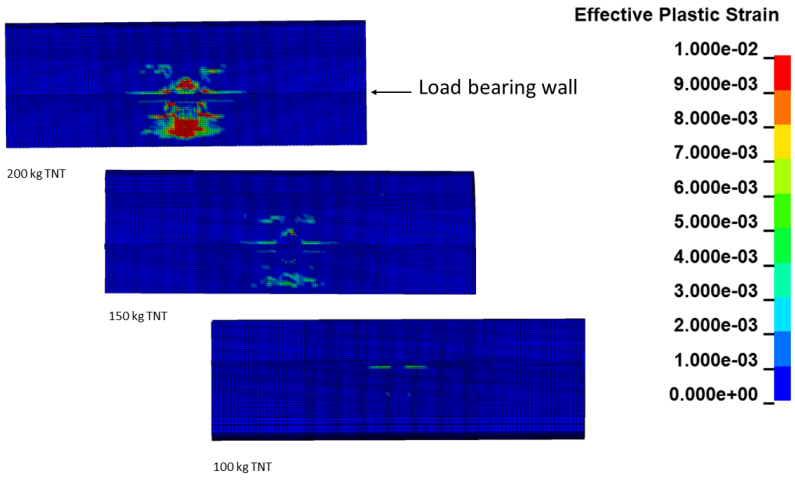

Figure 5.13: Contour plot of the effective plastic volumetric strain on the bottom side of the deck, 41 ms after detonation.

In addition to the effective plastic volumetric strain, Figure 5.9 presents the displacement in the y-direction, offering further insights into the effects of different charge sizes.

Notably, the charge size of 200 kg results in a significant displacement, indicating a substantial impact on the structural response. While the charge sizes of 100 kg and 150 kg exert minimal influence on the displacement, indicating relatively smaller magnitudes of deformation than the 200 kg charge size.

5.3 Results with Reinforcement

After analyzing the structural response of the internal concrete constructions, it was observed that the charge size of 200 kg TNT resulted in the most significant damage and displacement. Consequently, further investigations were focused solely on this charge size to evaluate the structural response of the internal constructions of reinforced concrete.

5.3.1 Structural Response

Figure 5.14 presents the contour plot depicting the displacement in the y-direction for the model with (left) and without (right) reinforcement. The inclusion of reinforcement in the structure leads to a significant reduction in displacement, as evident from the plot. This reduction is further highlighted by the maximum nodal displacement shown in Figure 5.15, where the deck with reinforcement exhibits a substantial decrease in nodal displacement.

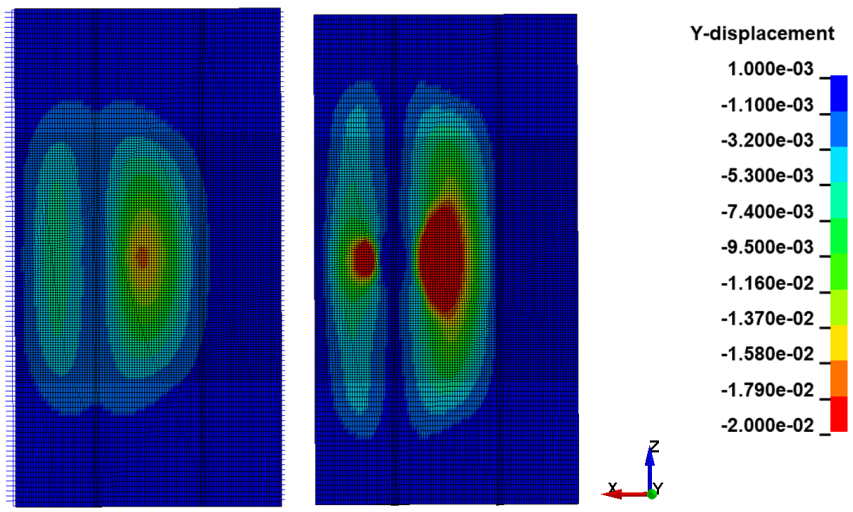

Figure 5.14: Displacement in y-direction for the model with (left) and without (right) reinforcement.

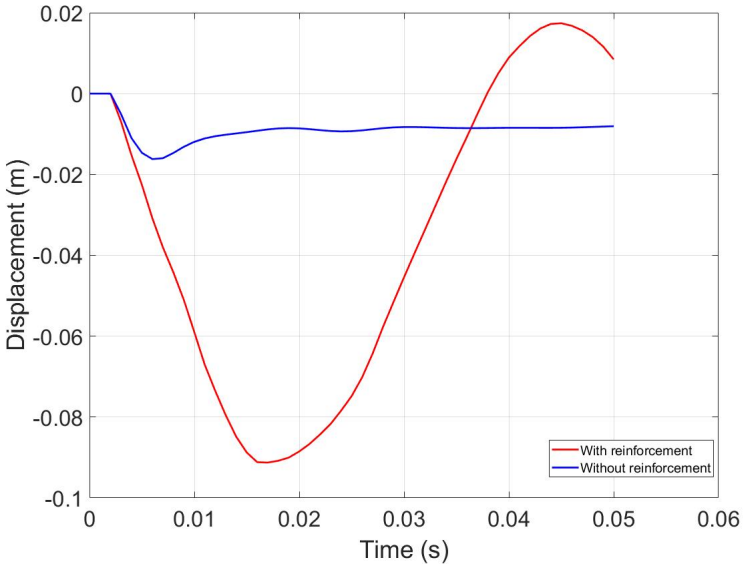

Figure 5.15: Nodal displacement for the model with (blue) and without reinforcement (red).

5.3.2 Stress and Strain Distribution

The contour plot displayed in Figure 5.16 visualizes the effective plastic volumetric strain for the deck with (left) and without (right) reinforcement. The inclusion of reinforcement has a notable impact on reducing plastic deformation by mitigating tensile stresses on the bottom surface of the deck. Nevertheless, in the model with reinforcement, there are localized strain concentrations near the connection of the deck and the load-bearing wall. These areas warrant further investigation to assess the need for additional reinforcement.

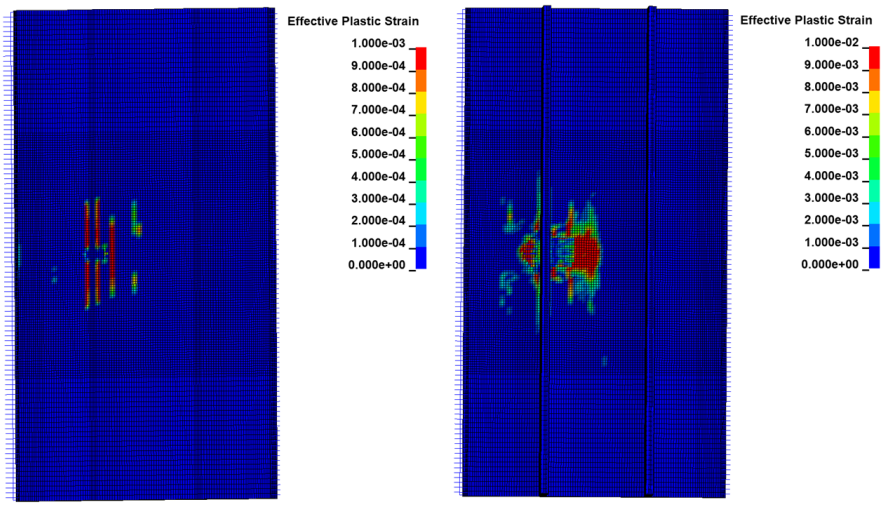

Figure 5.16: Contour plot of the effective plastic volumetric strain of the model with reinforcement (left) and without reinforcement (right) on the bottom side of the deck.

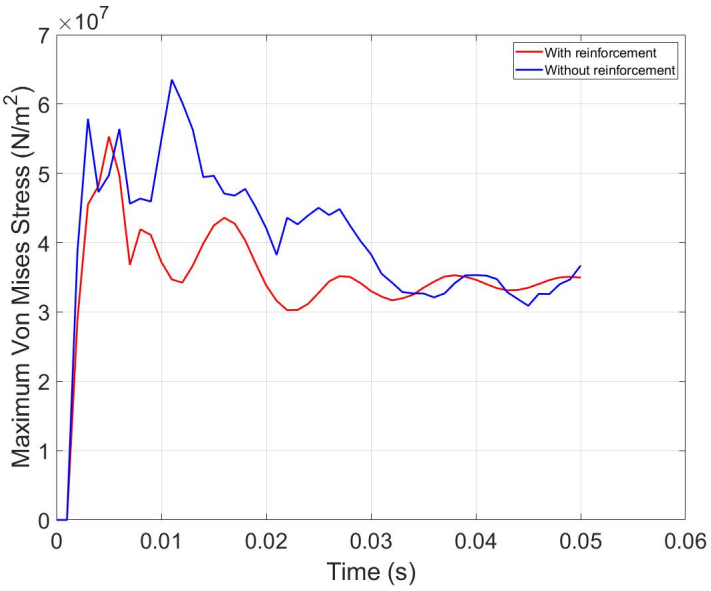

Figure 5.17: Maximum Von Mises Stress for the model with (red) and without (blue) reinforcement.

The reinforcement also reduces the maximum Von Mises stress value for the constructions as shown in Figure 5.17. Concrete, being a brittle material with limited tensile strength and energy absorption capacity, is susceptible to failure under blast loading. Consequently, the model that solely considers concrete exhibits higher Von Mises stress values compared to the reinforced model. The reinforcement effectively enhances the structural integrity and provides increased resistance against tensile stresses induced by the blast loading. Additionally, the reinforcement also distributes the stress more evenly throughout the structure. This can also be observed in Figure 5.17, with the round peaks in the graph.

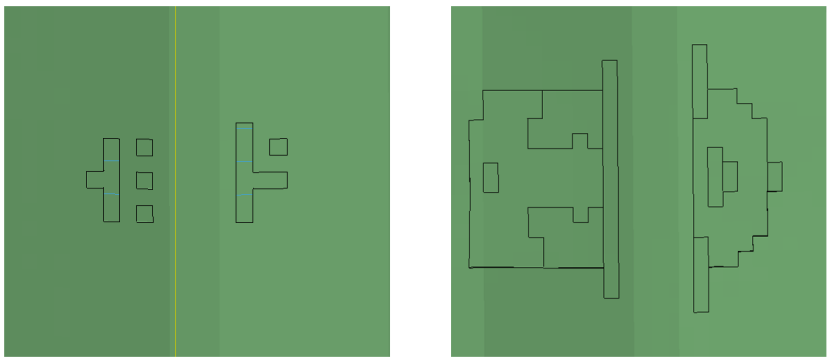

Figure 5.18: Element erosion with (left) and without (right) reinforcement.

5.3.3 Damage Assessment

Furthermore, the presence of reinforcement significantly reduces the visual damage caused by element erosion, as shown in Figure 5.18. This reduction can be attributed to the reinforcing bars' ability to enhance the concrete's resistance to tensile stresses. By reinforcing the concrete, the structural elements are better equipped to withstand and distribute the applied forces, resulting in a significant reduction in the extent of element erosion.

6 Numerical Model of Fire Damaged SFTB

During the service life of an SFTB, it may encounter fire and explosion events that could compromise its structural integrity. It is, therefore, crucial to investigate the impact of such incidents on the SFTB's overall blast resistance. This chapter aims to conduct test simulations of blast loading on the internal constructions of the SFTB, accounting for its reduced strength capacity from fire exposure.

6.1 Numerical Setup

This section provides a brief introduction to the numerical setup, and how the pre-existing damage by fire is simulated.

6.1.1 Material Setup After Fire Damage

A simplified approach was employed to simulate the pre-existing damage caused by fire. The reduction in strength caused by the high temperatures from fire was estimated based on previous studies conducted by Fletcher, Ian A. et al. ([39]) and Alhawat, Husen, et al. ([38]). Using the same material models as the intact SFTB, with adjusted strength values derived from the earlier research. It is important to note that this is a very simplified method, where the whole structure will have reduced strength capacity. In an actual fire incident, the temperature will not increase uniformly throughout the entire structure, which means this case study might not be reliable, but more of an indication.

6.1.1.1 Concrete and Steel Reinforcement

When the temperature reaches a certain point, the strength of construction materials starts to decrease (as earlier discussed in Section 3.3.2). According to Fletcher, Ian A. et al. ([39]) and Alhawat, Husen, et al. ([38]), the strength of steel will decrease with 80% at a temperature of 700°C, while the concrete will have a strength reduction of 55% at a temperature of 600°C. The reduced values for the concrete and steel reinforcement are presented in Table 6.1 and Table 6.2. Since the earlier research considers different temperatures, the reduction values are slightly reduced to compromise the temperature differences. Therefore, the compressive strength of the concrete is reduced by 50%, and

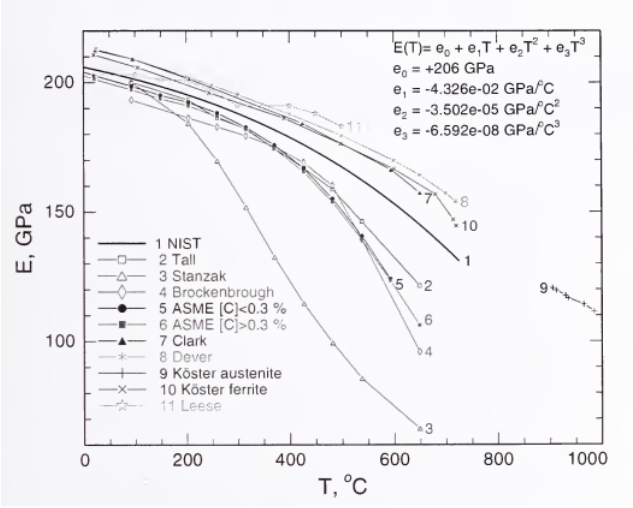

Figure 6.1: Young's modulus as a function of temperature [8].

the design strength of the steel is reduced by 70%. The difference in the stress-strain curve for the intact steel and the damaged steel is also illustrated in Figure 6.2.

For the steel reinforcement, the increasing temperature will also have an impact on Young's modulus (E-modulus). The E-modulus is usually between 190-210 GPa at room temperature, depending on the manufacturing process. Many determinations indicate the change of the E-modulus by the effect of increasing temperature, as illustrated in Figure 6.1. For this case, the evolution of the E-modulus was based on graph 1 NIST, at a temperature around 550 °C. Figure 6.1 shows that the E-modulus at 550°C will be around 170 GPa.

Table 6.1: Parameter inputs for CSCM concrete with reduced strength capacity corresponding to B45 concrete

Properties	**Value**
RO (Density, kg/m^3)	2400
NPLOT (Plotting option)	Plastic volume strain
INCRE (Max strain increment)	Default
IRATE (Rate effect option)	1 (on)
ERODE (Element erode time)	1.1
RECOV (Compression recovering)	Default
ITRETRC (Cap retraction option)	0 (Cap does not react)
PRED (Pre-existing damage)	0
FPC (Comressive strength, MPa)	22.5
DAGG (Max aggregate size, m)	0.022
UNITS (Units option)	Pa, m, sec, kg/m^3,N

Table 6.2: Parameter inputs for MAT024 with reduced strength capacity

Properties	**Value**
RO (Density, kg/m^3)	7800
E (Youngs modulus, N/m^2)	1.70e+11
PR (Poisson's ratio)	0.3
SIGY (Yield stress, N/m^2)	1.676e+08
ETAN (tengent modulus)	0 (Ignored)
FAIL (Failure flag)	0.25
TDEL (Minimum element deletation time step)	0
C (Strain rate parameter)	0
P (Strain rate parameter)	0

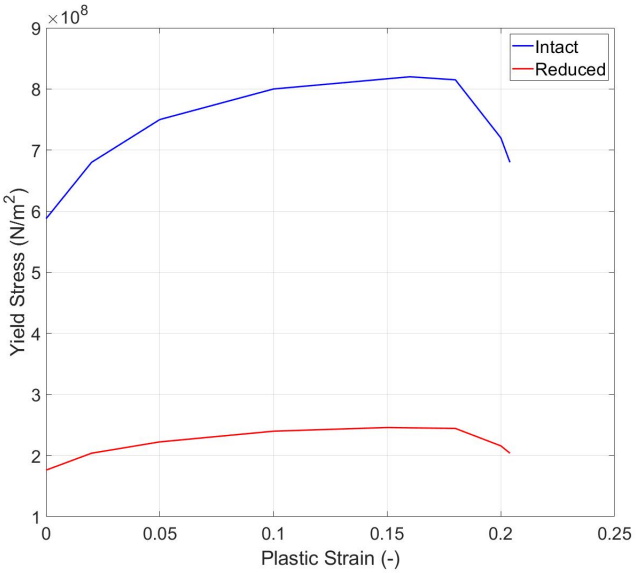

Figure 6.2: Yield stress and plastic strain curve for the design strength (blue) and reduced strength (red) of the steel.

6.1.1.2 Blast

In this case study, only one simulation with a charge size of 200 kg was conducted. The blast response of the damaged SFTB will be compared with the intact SFTB to get an insight into how the impact by fire will affect the blast response of the internal constructions. The explosion was situated in the exact location of the intact SFTB (see Figure 5.1)

6.1.2 Energy Balance

In the damaged model, similar to the intact model, an energy balance check was conducted. Figure 6.3 demonstrates that the hourglass energy comprises approximately 0.8% of the total energy, which falls well within the acceptable range. However, the energy ratio (Figure 6.4) exceeds 1 by approximately 7%, which is slightly higher than the recommended limit. As discussed in Chapter 5.1.5, the energy ratio should ideally not exceed 1 by more than +/- 0.05 (5%), although this is a guideline rather than an absolute limit. Consequently, it can be concluded that the energy ratio also falls within an acceptable range.

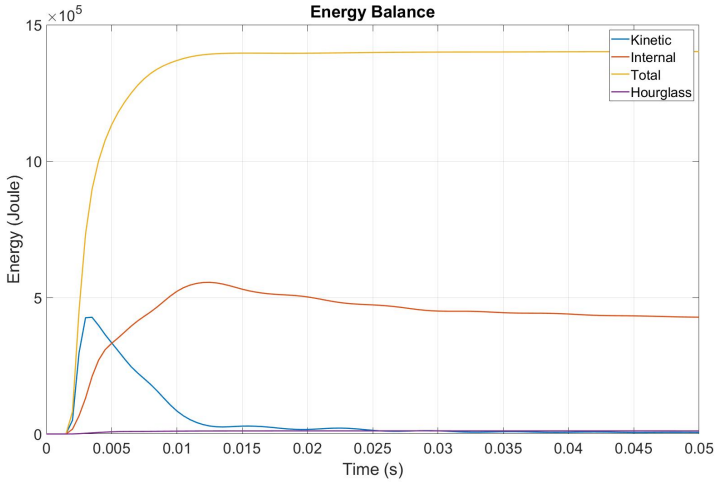

Figure 6.3: The development of total-, internal-, kinetic- and hourglass energy.

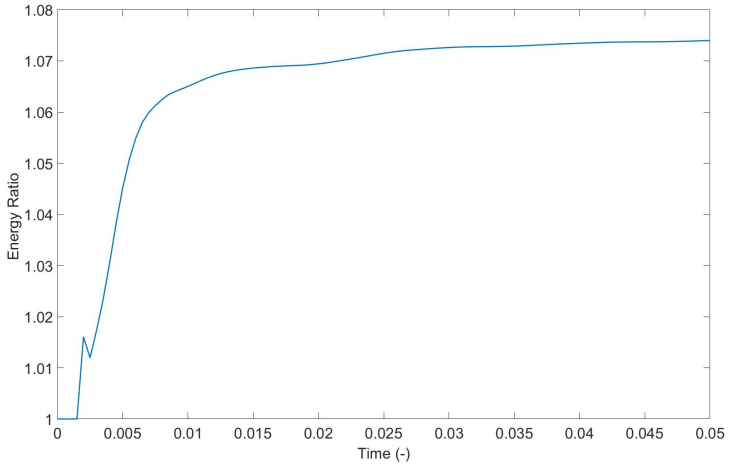

Figure 6.4: The energy ratio curve for the damaged model.

6.2 Results

Understanding the impact of fire on the blast resistance of an SFTB is essential for ensuring structural integrity and occupant safety. This section aims to assess the structural response of fire-damaged SFTBs by considering the fire-induced strength reduction in materials and conducting blast loading simulations.

Similar to the intact SFTB model, the damaged model required approximately two hours to run on an HPC system using 64 CPUs.

6.2.1 Effects of Pre-Existing Damage in CSCM Concrete

An attempt was made to account for fire damage using the "pre-existing damage" option in CSCM concrete. The pre-existing damage may vary from zero (default) to 1, and a value of 0.5 was chosen. The results in Figure 6.5 differed from expectations. Compared with no initial damage, less element erosion was observed but the effective plastic volumetric strain increased. It is difficult to pinpoint the reasons for this, and further investigation is out of the scope for this thesis. Nevertheless, the results highlight the importance of having in-depth knowledge of finite element modeling.

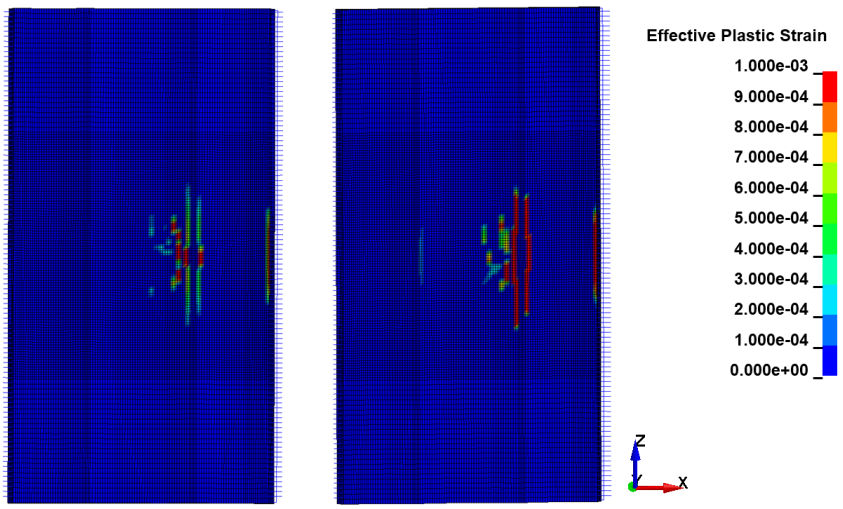

Figure 6.5: Contour plot of effective plastic volumetric strain. Reduced capacity by PRED variable (right) and by reducing the design strength for concrete and steel (left).

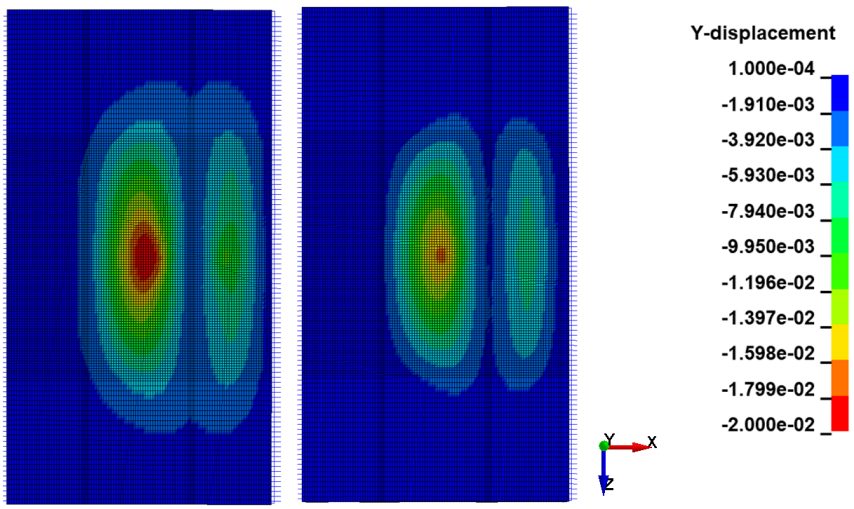

Figure 6.6: Contour plot of the displacement in y-direction for the damaged (left) and the intact (right) SFTB.

6.2.2 Load Propagation and Structural Response

The load propagation in the damaged model follows a pattern similar to that of the intact model. The blast wave originates from the detonation point and propagates towards the edges of the model, as depicted in Section 5.2.1, Figure 5.8.

Figure 6.6 compares the displacement of the intact and damaged models, revealing a significant disparity in displacement. The damaged model exhibits considerably higher maximum displacement, indicated by the red area. This is further highlighted by

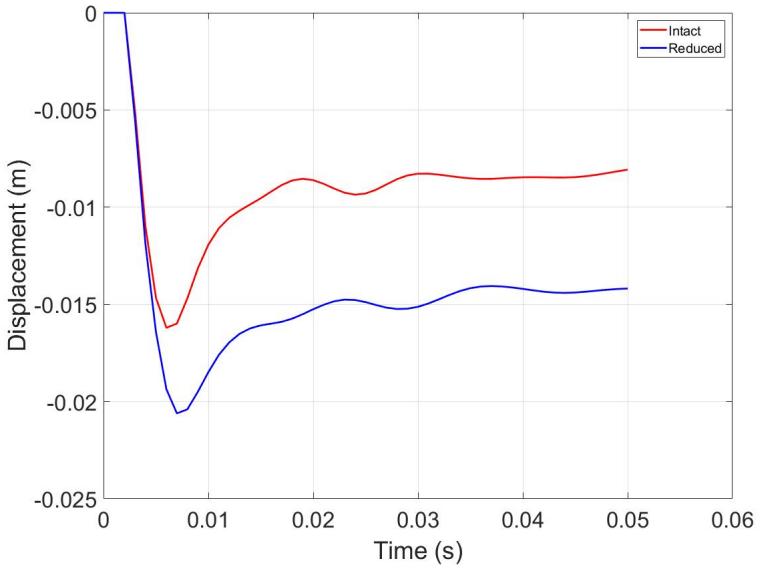

Figure 6.7: Nodal displacement in y-direction.

the maximum nodal displacement shown in Figure 6.7 (see Appendix A2 for nodal location). However, considering the reduced E-modulus and 70% reduced design strength of the reinforcement, along with the 50% reduced compressive strength, the difference in displacement was not as significant as anticipated.

6.2.3 Stress and Strain Distribution

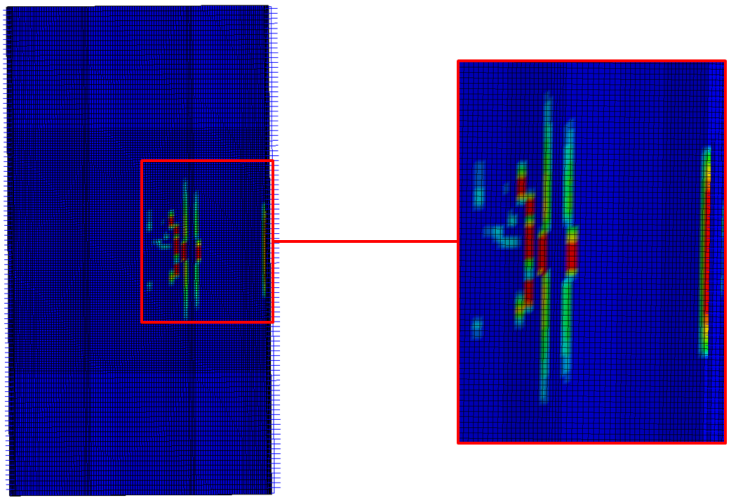

Figure 6.8: Contour plot of the effective plastic volumetric strain showcasing strain concentrations in the connection of the deck and tunnel wall.

The distribution of effective plastic volumetric strain on the bottom surface of the deck in the damaged model is illustrated in Figure 6.8. The contour plot indicates minimal plastic deformation in this region. However, localized strain concentrations are observed near the connections with the deck, load-bearing wall, and tunnel wall.

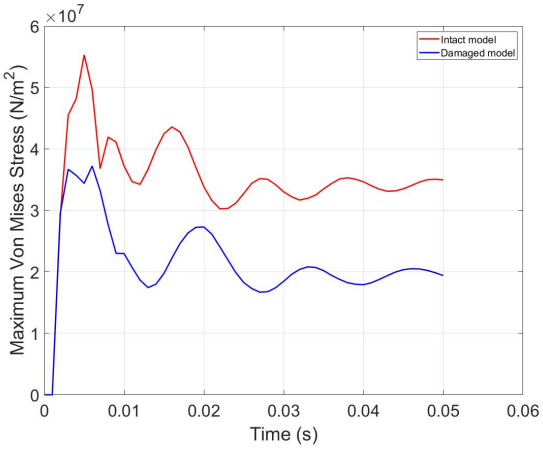

Figure 6.9: Maximum Von Mises stress for the damaged (blue) and the intact (red) model.

Figure 6.9 displays the maximum values of Von Mises stress. The damaged model is unable to withstand the same stresses as the intact model before yielding, which is expected.

6.2.4 Damage Assessment

Figure 6.10 visually represents the element erosion and resulting damage in the damaged and intact models. Surprisingly, the damaged model shows no signs of element erosion, while the intact model exhibits element erosion. This discrepancy raises doubts regarding the accuracy and validity of the simulation results for the damaged model, which will be further discussed in Section 7.2.

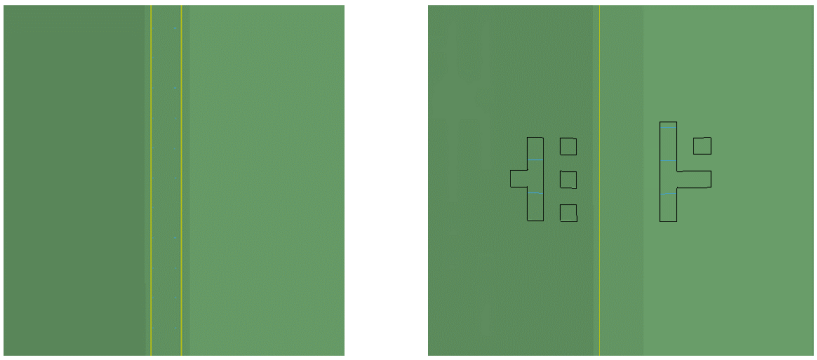

Figure 6.10: Element erosion on the bottom surface of the deck from the damaged model (left) and the intact model (right).

7 Discussion

In this chapter, the results of this present study will be discussed in detail. First, the results from the intact model with three different charge sizes, with and without reinforcement, will be discussed and compared. Then, the results from the damaged model will be discussed and compared to the reinforced intact model. Lastly, some important points in the preliminary study will be discussed.

7.1 The Intact Model

Firstly, it should be noted that the blast loads were located above a load-bearing wall. This placement can reduce displacement and damage, as the wall can absorb a significant portion of the blast energy due to its designed capacity to carry vertical loads. However, the response of structures to blast loads is complex and influenced by various factors, which is why the simulations, regardless of the placement, were not rerun.

The structural response of the SFTB's internal structures was evaluated under different charge sizes, considering both reinforced and unreinforced conditions. Surprisingly, none of the charge sizes damaged the main tunnel structure or the top surface of the deck, even in the absence of steel reinforcement. The deck did, however, experience element erosion on the bottom surface for all load cases. A possible explanation for this could be that the top surface was exposed to high compressive stresses while the bottom surface was exposed to high tensile stresses. It is essential to highlight that a more advanced blast model could have provided insight into additional damage, such as crack development and fragments on the top surface of the deck and the main structure. However, this aspect was not considered in this thesis.

The analysis of element erosion reveals a clear relationship between the size of the TNT charge and the resulting damage, underscoring the crucial role of reinforcement in reducing erosion by strengthening the concrete against tensile stresses. The charge size of 100 kg TNT had minimal impact on the erosion of unreinforced constructions, resulting in only a few elements being removed. While the damage caused by charge sizes of 150 kg and 200 kg to the deck was significantly larger, but it was less severe than expected, considering the absence of reinforcement. Interestingly, a previous study by Kristoffersen et al. ([11])

using the same cross section as this thesis reported damage to the internal structures with a 100 kg charge, while the main structure remained intact. It is challenging to pinpoint the exact reasons for the significant discrepancies in the results. Possible factors include materials, blast models, and software variations, as the research paper utilized ABAQUS with different settings compared to this thesis. Furthermore, the unknown span and mesh size of the model in the previous research might have influenced the divergent outcomes.

It was observed that the charge sizes of 100 kg and 150 kg had minimal impact on the plastic deformation of the unreinforced structures. This implies that the structural response under these charge sizes was relatively stable and did not result in significant deformations. The charge size of 200 kg did on the other hand have a large influence on the unreinforced deck. Specifically, the center of the deck emerged as the most vulnerable region, exhibiting the highest values of effective plastic volumetric strain. This suggests that the deck is particularly susceptible to deformation under higher blast loads.

The significance of reinforcement in reducing plastic deformation is evident from the comparison of the reinforced and unreinforced structures. With the incorporation of reinforcement, the plastic deformation was significantly reduced. Strain concentrations were observed primarily at the connections between the deck and the load-bearing wall, as well as the tunnel wall. This highlights the importance of reinforcement in enhancing structural integrity and distributing the applied loads more effectively. The impact of reinforcement is further supported by the analysis of nodal displacement, which clearly demonstrates the difference in deformation between reinforced and unreinforced constructions. The nodal displacement analysis emphasizes the effectiveness of reinforcement in minimizing deformations and improving the overall structural response.

7.2 The Fire Damaged Model

In the attempt to simulate concrete with pre-existing damage resulting from fire, two different approaches were examined. These approaches are outlined below:

1. By reducing the compressive strength of the concrete and reducing the design strength and the E-modulus of the steel reinforcement
2. By using the pre-existing parameter input in the concrete material model and by reducing the design strength and the E-modulus of the steel reinforcement

These two approaches produce unexpected results, particularly concerning element erosion. None of the tested approaches experienced any element erosion. These outcomes raise questions considering the significant reductions in strength and E-modulus implemented in the alternative approaches. One possible explanation lies in the concrete material model, where interconnected parameters like strain rate sensitivity, E-modulus, and tensile strength are linked to the compressive strength input. These interdependencies may have influenced the critical value for element erosion. Therefore, an improved alternative could be to use the *MAT_159_CSCM material model instead of the *MAT_159_CSCM_CONCRETE. The *MAT_159_CSCM model allows for defining concrete properties independently, reducing compressive strength without compromising parameters like strain rate sensitivity, tensile strength, and E-modulus. However, the outcome displayed higher nodal and overall displacement, which makes the lack of element erosion even more puzzling considering the increased tensile stresses on the bottom surface of the deck.

Another unexpected outcome was observed in terms of plastic deformation. Although the damaged model exhibited some plastic deformation, the extent of deformation was comparable to that of the intact reinforced model subjected to a 200 kg TNT detonation. This result can also be attributed to the selection of the material model and the interdependencies among its parameters. The Von Mises stress results, however, aligned with expectations, indicating that the structure was unable to withstand the same level of stress as the intact model before yielding.

7.3 Preliminary Study

The preliminary study on the material and blast models yielded satisfactory results for the intact model. However, it is essential to acknowledge the limitation of not conducting similar tests on concrete with pre-existing damage. Examining the behavior of the concrete with reduced compressive strength and incorporating the pre-existing damage parameter could have provided valuable insights into its response under such conditions. This additional analysis would have allowed for a more comprehensive understanding of how the concrete material would have behaved in the presence of pre-existing damage. Although this aspect was not explored in the current study, it is recommended that future research considers incorporating these tests further to enhance the accuracy and applicability of the findings.

8 Conclusion and Further Work

8.1 Conclusion

This thesis utilized LS-DYNA to examine the structural response to blast loading and the combined effects of blast loading and fire impact. The study yielded diverse results through numerical simulations involving three different charge sizes. Based on these findings, the following conclusion can be drawn.

In the intact model, it was observed that none of the tested charge sizes caused any significant damage to the main tunnel structure or the top surface of the deck. However, element erosion was observed on the bottom surface of the deck, which can be attributed to the differential loading conditions between the top and bottom surfaces. These findings prompt further discussion on the structural response to blast loads. The results also highlight the need for advanced blast models to capture more complex damage mechanisms and crack development. These insights contribute to understanding structural behavior under blast loads and pave the way for future research and improvements in blast-resistant design.

The results also raise questions regarding simulating the behavior of damaged structures under blast loads. The unforeseen outcomes and unexpected behaviors observed in the tested alternatives emphasize the importance of comprehensively understanding the concrete material model and the complex interactions among various structural parameters. Such understanding is crucial for accurately predicting and assessing a damaged structure's response to explosive forces.

Before implementation, further research is necessary to understand the complex nature of internal blast loading in SFTBs. In this regard, a solid understanding of finite element modeling is essential for conducting accurate simulations that capture non-linear behavior. Furthermore, it is crucial to carefully analyze the results and observe any discrepancies in the model to ensure the validity of the findings.

Throughout the semester, the researcher has acquired extensive knowledge of the effects of blast loading on structural response. In addition, a capable understanding of the LS-DYNA software has been developed, encompassing both the model creation process

and the pre-processing of results. Overall, this thesis project has been a challenging and captivating experience, fostering personal growth.

8.2 Further work

Recommendations for further investigation of the structural response of internal blast loading in SFTBs may be:

- Examining the default concrete material model with pre-existing damage to gain a better understanding of its behavior and the interdependencies among its parameters.
- Investigating the dynamic response of the reinforcement to assess its influence on the structural behavior under blast loading.
- Investigating more advanced blast models to capture additional damage mechanisms and crack development.
- Examining the structural response of other cross sections under combined explosion and fire loading conditions to broaden the applicability of the findings.
- Considering the use of Computational Fluid Dynamics (CFD) to simulate the fire and smoke in an SFTB, enabling a comprehensive assessment of the combined blast and fire effects.

Acknowledgement

The simulations were performed on resources provided by Sigma2 - the National Infrastructure for High Performance Computing and Data Storage in Norway.

References

[1] K. K. Dunham, "Coastal highway route e39–extreme crossings," *Transportation research procedia*, 2016.

[2] U.S. ARMY CORPS OF ENGINEERS, NAVAL FACILITIES ENGINEERING COMMAND, AIR FORCE CIVIL ENGINEER SUPPORT AGENCY, *STRUCTURES TO RESIST THE EFFECTS OF ACCIDENTAL EXPLOSIONS UFC 3-340-02*, UNIFIED FACILITIES CRITERIA, USA, 2008. [Online]. Available: https://www.wbdg.org/FFC/DOD/UFC/ARCHIVES/ufc_3_340_02.pdf

[3] K. A. M. Edward J. Conrath, Ted Krauthammer and P. F. Mlakar, *Structural Design For Physical Secturity State of the Practice*. SEI, 1999.

[4] Y. Shi, H. Hao, and Z.-X. Li, "Numerical derivation of pressure–impulse diagrams for prediction of rc column damage to blast loads," *International Journal of Impact Engineering*, 2008.

[5] A. Filice, M. Mynarz, and R. Zinno, "Experimental and empirical study for prediction of blast loads," *Applied Sciences*, 2022.

[6] *Eurokode 1: Laster på konstruksjoner Del 1-7: Allmenne laster Ulykkeslaster*, Standard Norge, Oslo, Norge, 2008.

[7] M. Kristoffersen, K. O. Hauge, A. Minoretti, and T. Børvik, "Experimental and numerical studies of tubular concrete structures subjected to blast loading," *Engineering Structures*, 2021.

[8] W. E. Luecke, W. E. Luecke, J. D. McColskey, C. N. McCowan, S. W. Banovic, R. J. Fields, T. Foecke, T. A. Siewert, and F. W. Gayle, *Mechanical properties of structural steels*. National Institute of Standards and Technology, Technology Administration . . . , 2005.

[9] NPRA, "Feasibility study for crossing the sognefjord," 2012.

[10] A. Minoretti, E. M. Egeland, and T. E. Aasland, "The submerged floating tube bridge for the norwegian fjords," in *The 29th International Ocean and Polar Engineering Conference*. OnePetro, 2019.

[11] M. Kristoffersen, A. Minoretti, and T. Børvik, "On the internal blast loading of submerged floating tunnels in concrete with circular and rectangular cross-sections," *Engineering failure analysis*, 2019.

[12] M. Kristoffersen, K. O. Hauge, and T. Børvik, "Blast loading of concrete pipes using c-4 charges," in *Proceedings*. MDPI, 2018.

[13] R. Cheng, W. Chen, H. Hao, and J. Li, "A state-of-the-art review of road tunnel subjected to blast loads," *Tunnelling and Underground Space Technology*, 2021.

[14] T. Chakraborty, M. Larcher, and N. Gebbeken, "Performance of tunnel lining materials under internal blast loading," *International Journal of Protective Structures*, 2014.

[15] J. Li, H. Hao, W. Chen, and R. Cheng, "Calculation of bleve energy and overpressures inside a tunnel using analytical and cfd methods," *Tunnelling and Underground Space Technology*, 2022.

[16] M. H. Mussa, A. A. Mutalib, R. Hamid, S. R. Naidu, N. A. M. Radzi, and M. Abedini, "Assessment of damage to an underground box tunnel by a surface explosion," *Tunnelling and underground space technology*, 2017.

[17] R. Cheng, W. Chen, H. Hao, and J. Li, "Effect of internal explosion on tunnel secondary and adjacent structures: A review," *Tunnelling and Underground Space Technology*, 2022.

[18] M. Colombo, P. Martinelli, and M. di Prisco, "A design approach for tunnels exposed to blast and fire," *Structural Concrete*, 2015.

[19] Y. Shen, J. Ling, W. Wang, H. Zhu, and Z. Yan, "3d numerical investigation on response of shield tunnel under combined effects of fire and structural loading," *Tunnelling and Underground Space Technology*, 2022.

[20] N. Hua, N. E. Khorasani, and A. Tessari, "Numerical modeling of the fire behavior of reinforced concrete tunnel slabs during heating and cooling," *Engineering Structures*, 2022.

[21] I. Almeshal, B. Abu Bakar, and B. A. Tayeh, "Behaviour of reinforced concrete walls under fire: a review," *Fire Technology*, 2022.

[22] D. Qin, P. Gao, F. Aslam, M. Sufian, and H. Alabduljabbar, "A comprehensive review on fire damage assessment of reinforced concrete structures," *Case Studies in Construction Materials*, 2022.

[23] T. Roy and V. Matsagar, "A probabilistic framework for assessment of reinforced concrete wall panel under cascaded post-blast fire scenario," *Journal of Building Engineering*, 2022.

[24] Z. Xu, J. Li, and C. Wu, "A numerical study of blast resistance of fire damaged ultra-high performance concrete columns," *Engineering Structures*, 2023.

[25] B. Jakobsen, "Design of the submerged floating tunnel operating under various conditions," *Procedia Engineering*, 2010.

[26] Sha, Yanyan, *Lecture 2-Blast waves*, Analyse og dimensjonering av stålkonstruksjoner: Videregående, Norway, 2022.

[27] C. E. Needham, D. Ritzel, G. T. Rule, S. Wiri, and L. Young, "Blast testing issues and tbi: experimental models that lead to wrong conclusions," *Frontiers in neurology*, 2015.

[28] D. A. Crowl, *Understanding explosions*. John Wiley & Sons, 2010.

[29] P. Shirbhate and M. Goel, "A critical review of blast wave parameters and approaches for blast load mitigation," *Archives of Computational Methods in Engineering*, 2021.

[30] C. N. Kingery and G. Bulmash, *Airblast parameters from TNT spherical air burst and hemispherical surface burst*. US Army Armament and Development Center, Ballistic Research Laboratory, 1984.

[31] D. Hou and Q. Li, "Damage boundaries on shock response spectrum based on an elastic single-degree-of-freedom structural model," *International Journal of Impact Engineering*, 2023.

[32] SIMULIA, "Abaqus analysis user's manual version 2019," 2018.

[33] E. Krone, "Internal blast loading of submerged floating tunnels in concrete," Master's thesis, NTNU, 2018.

[34] R. D. Cook, D. S. Malkus, M. E. Plesha, and R. J. Witt, *Concepts and applications of finite element analysis*. Wiley, 2001.

[35] University of Memphis, *Lecture notes in CIVL 1101 - Civil Engineering Measurements: Properties of Concrete*. [Online]. Available: http://www.ce.memphis.edu/1101/notes/concrete/section_3_properties.html

[36] P. Taylor, E. Yurdakul, H. Ceylan, F. Bektas *et al.*, "Development of performance properties of ternary mixtures and concrete pavement mixture design and analysis (mda): effect of paste quality on fresh and hardened properties of ternary mixtures." Iowa State University. Institute for Transportation, Tech. Rep., 2012.

[37] Y. D. Murray *et al.*, "Users manual for ls-dyna concrete material model 159," United States. Federal Highway Administration. Office of Research ..., Tech. Rep., 2007.

[38] H. Alhawat, R. Hamid, S. Baharom, M. Azmi, and A. Kaish, "Thermal behavior of unloaded concrete tunnel lining through an innovative large-scale tunnel fire experimental testing setup," *Construction and Building Materials*, 2021.

[39] I. A. Fletcher, S. Welch, J. L. Torero, R. O. Carvel, and A. Usmani, "Behaviour of concrete structures in fire," *Thermal science*, 2007.

[40] R. Kuehnen, M. A. Youssef, and S. F. El-Fitiany, "Influence of natural fire development on concrete compressive strength," *Fire*, 2022.

[41] Sha, Yanyan, *Lecture 8-Nonlinear Finite Element Analysis (NLFEA) for ALS*, Analyse og dimensjonering av stålkonstruksjoner: Videregående, Norway, 2022.

[42] DYNAMORE, "Time step size," 2023.

[43] A. Antoniou, T. Børvik, and M. Kristoffersen, "Evaluation of automatic versus material test-based calibrations of concrete models for ballistic impact simulations," *International Journal of Protective Structures*, 2023.

[44] L. Schwer, H. Teng, and M. Souli, "Ls-dyna air blast techniques: comparisons with experiments for close-in charges," in *10th European LS-DYNA Conference, Würzburg, Germany*, 2015.

[45] L.-D. LSTC, "Keyword user's manual volume ii-material models," 2013.

[46] DynaMore, "Constrained beam in solid," Unknown.

[47] LS-DYNA, "Introduction to ls-dyna," Unknown.

[48] ABAQUS, "Lecture 1: Overview of abaqus/explicit," 2005.

Appendix

A Theory

A1 Blast Load

D.3 Eksplosjoner i veg- og jernbanetunneller

(1) I tilfelle detonasjon i veg- og jernbanetunneler kan funksjonen for sammenhengen mellom trykk og tid bestemmes ved hjelp av uttrykk (D.7) til (D.9), se figur D.1(a):

$$p(x,t) = p_0 \exp\left\{-\left(t - \frac{|x|}{c_1}\right)/t_0\right\} \text{ for } \frac{|x|}{c_1} \le t \le \frac{|x|}{c_2} - \frac{|x|}{c_1} \quad \text{(D.7)}$$

$$p(x,t) = p_0 \exp\left\{-\left(\frac{|x|}{c_2} - 2\frac{|x|}{c_1}\right)/t_0\right\} \text{ for } \frac{|x|}{c_2} - \frac{|x|}{c_1} \le t \le \frac{|x|}{c_2} \quad \text{(D.8)}$$

$$p(x,t) = 0 \text{ for alle andre forhold} \quad \text{(D.9)}$$

der

p_0 er topptrykket (= 2 000 kN/m^2 for et typisk flytende naturgassbrensel);

C_1 er forplantningshastigheten for sjokkbølgen (~ 1 800 m/s);

C_2 er den akustiske spredningshastigheten i varme gasser (~ 800 m/s);

t_0 er tidskonstanten (= 0,01 s);

$|x|$ er avstanden til sentrum av eksplosjonen;

t er tidsrommet.

(2) I tilfelle deflagrasjon i veg- og jernbanetunneler kan følgende karakteristiske sammenheng mellom trykk og tid vurderes, se figur D1(b):

$$p(t) = 4p_0 \frac{t}{t_0}\left(1 - \frac{t}{t_0}\right) \text{ for } 0 \le t \le t_0 \quad \text{(D.10)}$$

der

p_0 er topptrykket (=100 kN/m^2 for et typisk flytende naturgassbrensel);

t_0 er tidskonstanten (= 0.1 s);

t er tiden.

(3) Trykket bestemt ut fra uttrykk (D.10) kan brukes for hele den innvendige overflaten i tunnelen.

Figure A1.1: Empirical equations from EC 1-7 [6].

B Numerical Model

A1 Technical Drawings from NPRA

The technical drawings from NPRA are illustrated below.

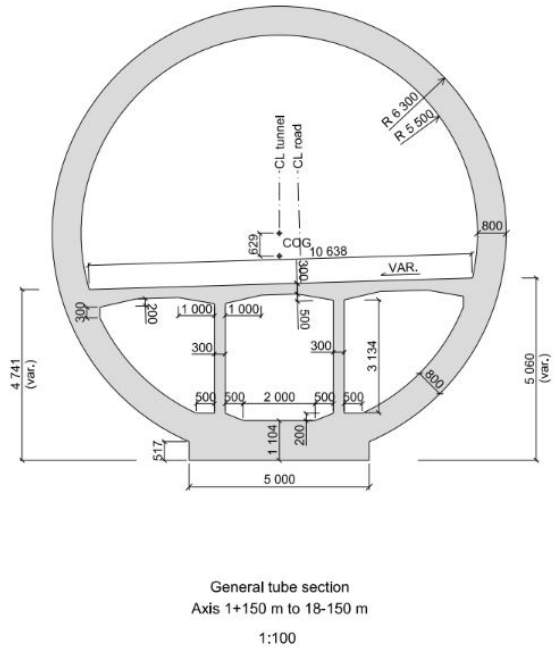

Figure A1.1: Technical drawing of the SFTB geometry [9].

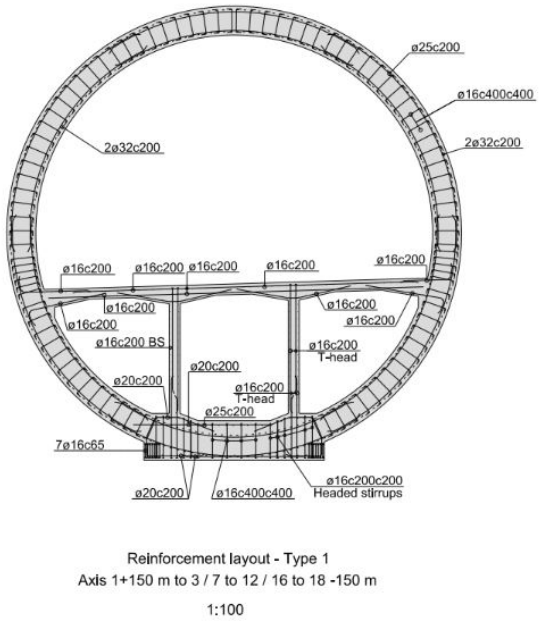

Figure A1.2: Technical drawing of the SFTB reinforcement [9].

A2 Nodal Displacement

The exact location of the nodal displacement discussed in Section 5.2.2 and Section 6.2.2 are depicted below.

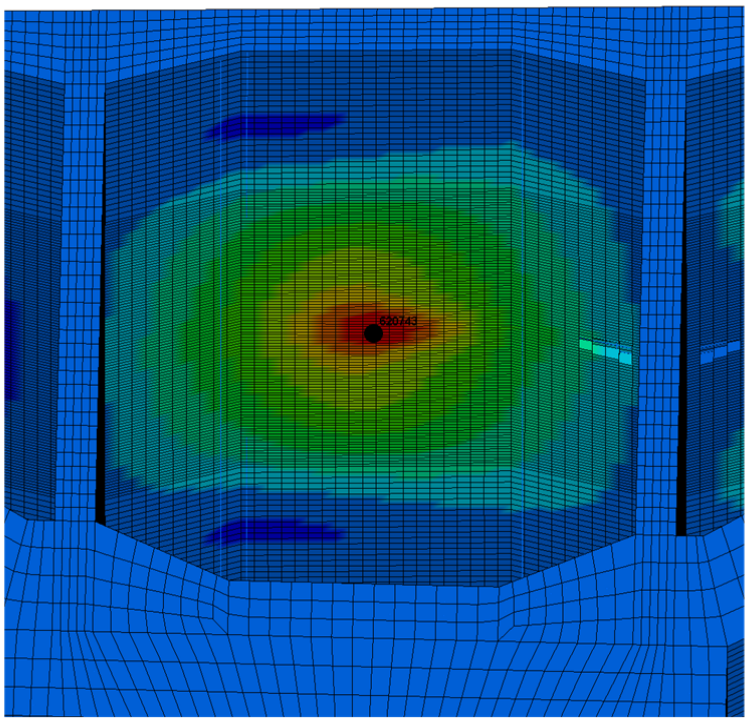

Figure A2.1: Exact location of maximum nodal displacement from 100 kg TNT detonation on the unreinforced model (node id 620743).

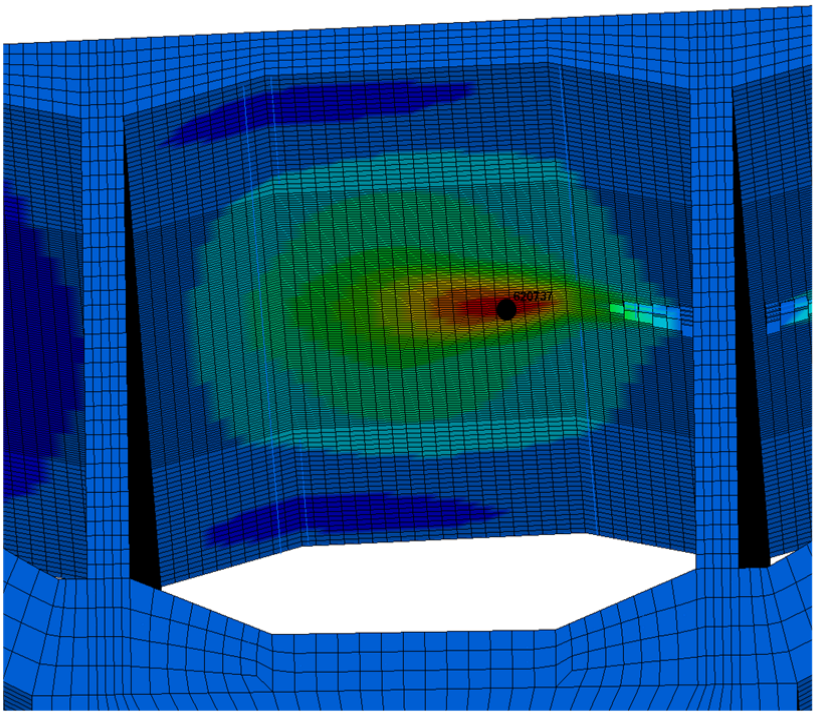

Figure A2.2: Exact location of maximum nodal displacement from 150 kg TNT detonation on the unreinforced model (node id 620734).

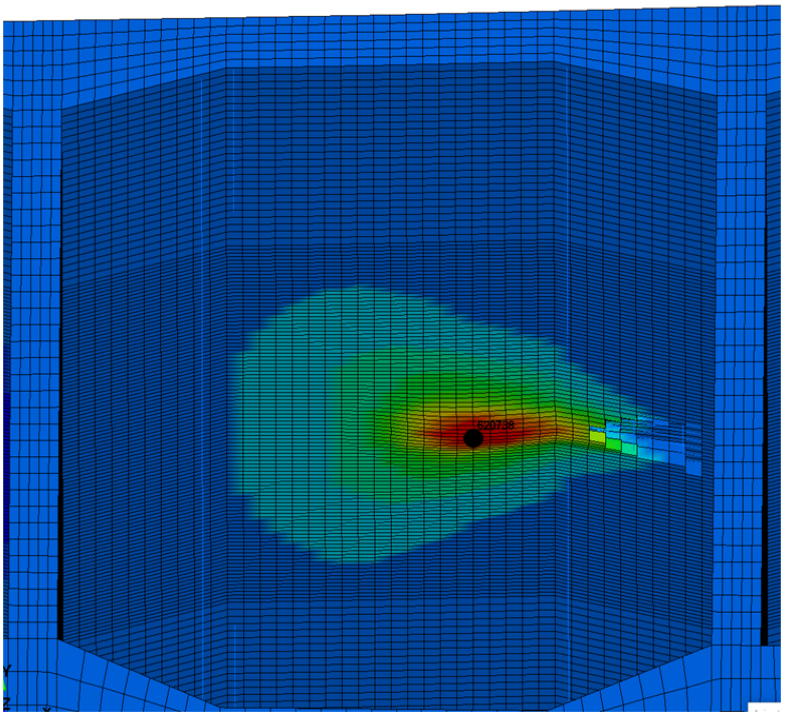

Figure A2.3: Exact location of maximum nodal displacement from 200 kg TNT detonation on the unreinforced model (node id 620738).

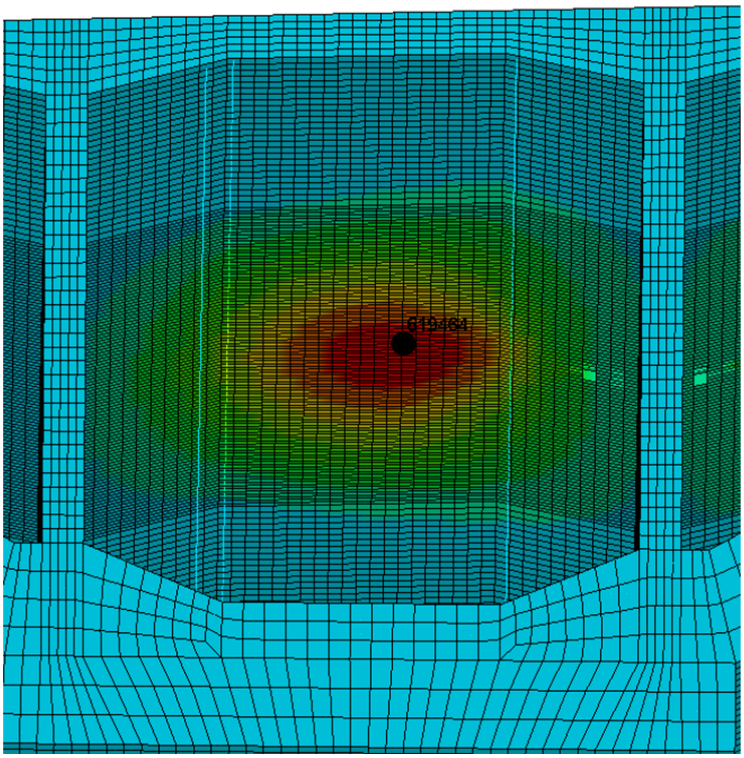

Figure A2.4: Exact location of maximum nodal displacement from 200 kg TNT detonation on the reinforced model (node id 619464).

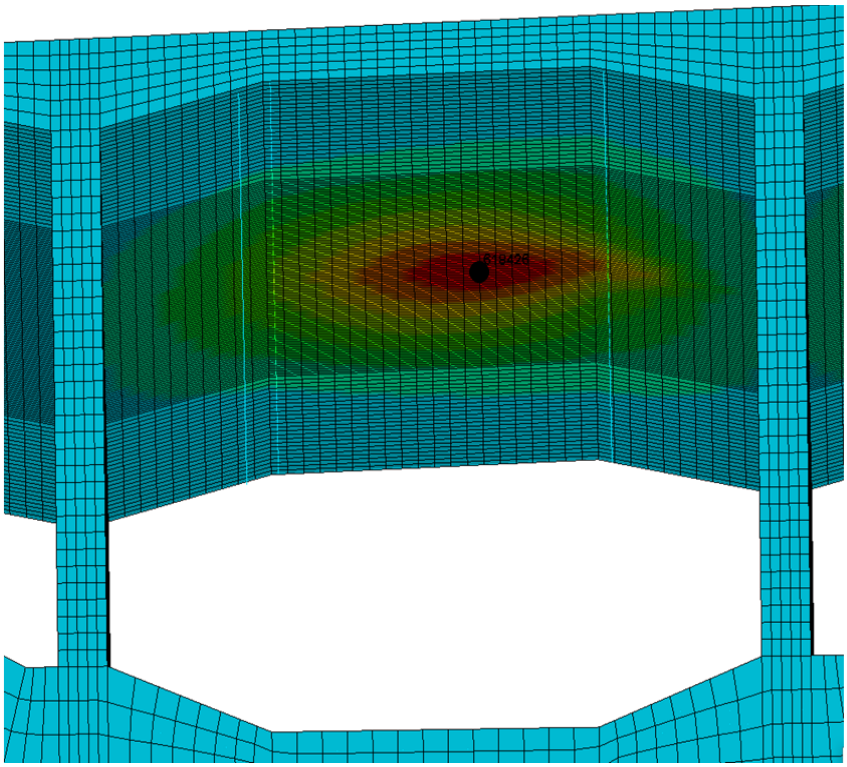

Figure A2.5: Exact location of maximum nodal displacement from 200 kg TNT detonation on the damaged model (node id 618426).

A3 Keyword-file

The keyword file for the blast model is depicted in Figure A3.1.

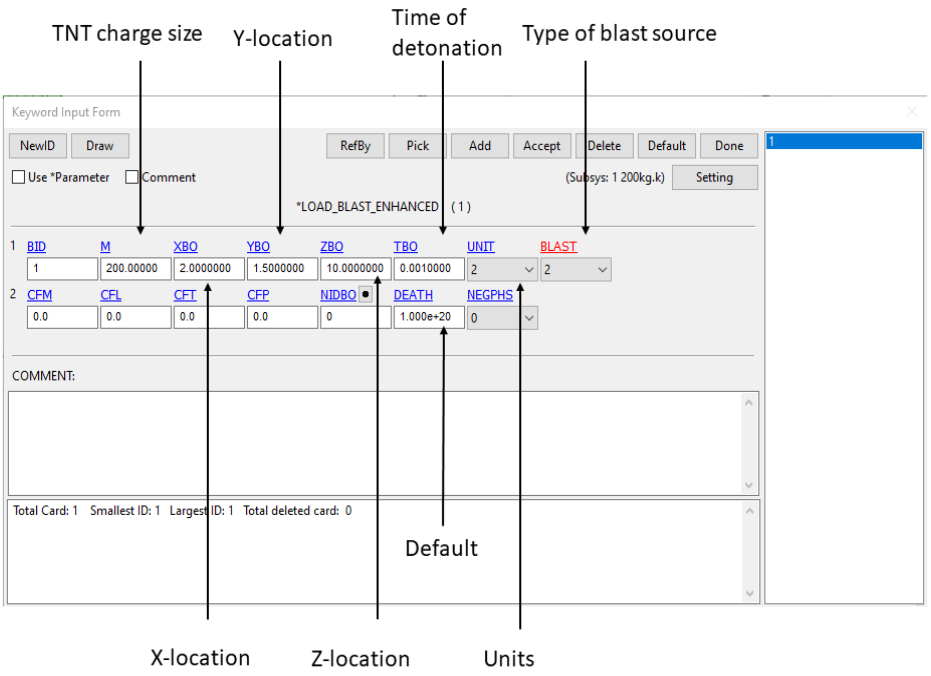

Figure A3.1: LOAD_BLAST_ENHANCED keyword.